

A positive feedback loop between Flower and PI(4,5)P₂ at periaxial zones controls bulk endocytosis in *Drosophila*

Tsai-Ning Li¹, Yu-Jung Chen¹, Ting-Yi Lu¹, You-Tung Wang¹, Hsin-Chieh Lin¹, Chi-Kuang Yao^{1,2,3*}

¹Institute of Biological Chemistry, Academia Sinica, Taipei, Taiwan; ²Neuroscience Program of Academia Sinica, Academia Sinica, Taipei, Taiwan; ³Institute of Biochemical Sciences, College of Life Science, National Taiwan University, Taipei, Taiwan

Abstract Synaptic vesicle (SV) endocytosis is coupled to exocytosis to maintain SV pool size and thus neurotransmitter release. Intense stimulation induces activity-dependent bulk endocytosis (ADBE) to recapture large quantities of SV constituents in large endosomes from which SVs reform. How these consecutive processes are spatiotemporally coordinated remains unknown. Here, we show that Flower Ca²⁺ channel-dependent phosphatidylinositol 4,5-bisphosphate (PI(4,5)P₂) compartmentalization governs control of these processes in *Drosophila*. Strong stimuli trigger PI(4,5)P₂ microdomain formation at periaxial zones. Upon exocytosis, Flower translocates from SVs to periaxial zones, where it increases PI(4,5)P₂ levels via Ca²⁺ influxes. Remarkably, PI(4,5)P₂ directly enhances Flower channel activity, thereby establishing a positive feedback loop for PI(4,5)P₂ microdomain compartmentalization. PI(4,5)P₂ microdomains drive ADBE and SV reformation from bulk endosomes. PI(4,5)P₂ further retrieves Flower to bulk endosomes, terminating endocytosis. We propose that the interplay between Flower and PI(4,5)P₂ is the crucial spatiotemporal cue that couples exocytosis to ADBE and subsequent SV reformation.

*For correspondence: ckyao@gate.sinica.edu.tw

Competing interests: The authors declare that no competing interests exist.

Funding: See page 20

Received: 17 June 2020

Accepted: 09 December 2020

Published: 10 December 2020

Reviewing editor: Hugo J Bellen, Baylor College of Medicine, United States

© Copyright Li et al. This article is distributed under the terms of the [Creative Commons Attribution License](https://creativecommons.org/licenses/by/4.0/), which permits unrestricted use and redistribution provided that the original author and source are credited.

Introduction

Proper synaptic vesicle (SV) exocytosis dictates the robustness of brain activity. Coupling SV exocytosis with proper endocytosis is crucial for maintaining a balance of SV proteins at the release site, plasma membrane equilibrium, SV identity, and SV pool size (*Chanaday et al., 2019; Haucke et al., 2011; Lou, 2018; Wu et al., 2014a*). Currently, four modes of SV endocytosis are proposed. These differ in terms of stimulation intensity for their induction, formation, and molecular components (*Haucke et al., 2011; Kononenko and Haucke, 2015; Wu et al., 2014a*). Under mild neuronal stimulation, the SV partially fuses with the plasma membrane and reforms at the active zone, the so called 'kiss and run' mode. During clathrin-mediated endocytosis (CME), the SV fully collapses into the plasma membrane, followed by reformation of a single SV. Ultrafast endocytosis was also shown to recycle SVs at a sub-second timescale by forming a ~ 80 nm-sized bulk endosome predominantly at the edge of the active zone. SVs subsequently regenerate from this bulk endosome (*Granseth et al., 2006; Watanabe et al., 2013a; Watanabe et al., 2013b; Zhu et al., 2009*). High frequency stimulation and thus exocytosis could easily surpass the capacity of the three above-described endocytic mechanisms. It has therefore been proposed that activity-dependent bulk endocytosis (ADBE) has the necessary recapture capacity upon intense stimulation (*Clayton et al., 2008; Soykan et al., 2017; Wu and Wu, 2007*). This retrieval mode is elicited at the periaxial zone to recapture large quantities of SV constituents via bulk endosome (~100–500 nm) formation, from which SVs subsequently reform. Hence, specific routes of SV recycling may fit the specific demands

of a wide range of neuronal activities at the synapse. However, how stimulation intensity dictates the choice between these different endocytic modes is not well understood.

ADBE has been documented in many different types of neurons in invertebrates and vertebrates (Clayton *et al.*, 2008; Heerssen *et al.*, 2008; Heuser and Reese, 1973; Holt *et al.*, 2003; Kasprowicz *et al.*, 2008; Kittelmann *et al.*, 2013; Miller and Heuser, 1984; Richards *et al.*, 2000; Soykan *et al.*, 2017; Stevens *et al.*, 2012; Vijaykrishnan *et al.*, 2009; Wenzel *et al.*, 2012; Wu and Wu, 2007; Yao *et al.*, 2017). Although the precise mechanism regulating ADBE is not known, multiple lines of evidence suggest that actin polymerization may serve as the membrane invagination force responsible for generating bulk endosomes (Gormal *et al.*, 2015; Holt *et al.*, 2003; Kokotos and Low, 2015; Nguyen *et al.*, 2012; Richards *et al.*, 2004; Soykan *et al.*, 2017; Wu *et al.*, 2016). Furthermore, phosphatidylinositol metabolism has also been implicated in controlling this recycling mode (Gaffield *et al.*, 2011; Holt *et al.*, 2003; Richards *et al.*, 2004; Vijaykrishnan *et al.*, 2009). Importantly, loss of Synaptojanin, the major phosphatidylinositol 4,5-bisphosphate (PI(4,5)P₂) catalytic enzyme in neurons (Tsujiyama *et al.*, 2001), leads to reduced SV endocytosis elicited by intense stimulation, presumably by affecting ADBE (Mani *et al.*, 2007). PI(4,5)P₂ is known to promote actin polymerization by activating a number of actin modulators (Janmey *et al.*, 2018). PI(4,5)P₂ is clustered to form microdomains upon the demand for diverse cellular functions (Aoyagi *et al.*, 2005; Chen *et al.*, 2015; Honigmann *et al.*, 2013; Kabeche *et al.*, 2015; Mu *et al.*, 2018; Picas *et al.*, 2014; Riggi *et al.*, 2018; van den Bogaart *et al.*, 2011). It has also been reported that formation of PI(4,5)P₂ microdomains precedes actin polymerization during a process reminiscent of ADBE in neurosecretory cells (Gormal *et al.*, 2015). Thus, subcellular compartmentalization of PI(4,5)P₂ may provide the spatial information dictating where bulk membranes will invaginate. However, the mechanism initiating the formation of the PI(4,5)P₂ microdomains is unknown.

Coordinated SV protein and membrane retrieval plays an important role in maintaining the identity of newly formed SVs during SV recycling (Kaempf and Maritzen, 2017; McMahon and Boucrot, 2011; Saheki and De Camilli, 2012; Traub and Bonifacino, 2013). It has been well documented that proper sorting of SV proteins to the nascent SV is achieved in CME by the cooperative action of PI(4,5)P₂ and adaptor protein complexes (Saheki and De Camilli, 2012; Traub and Bonifacino, 2013). Recent studies have also revealed a distinct sorting mechanism that retrieves selective SV cargoes to the bulk endosome via ADBE (Kokotos *et al.*, 2018; Nicholson-Fish *et al.*, 2015). Several lines of evidence further suggest that clathrin and adaptor protein complexes are required for reforming SVs from the bulk endosome (Cheung and Cousin, 2012; Glyvuk *et al.*, 2010; Kokotos *et al.*, 2018; Kononenko *et al.*, 2014; Park *et al.*, 2016). A dynaminI/dynaminIII/clathrin-independent mechanism has also been reported as being involved in this process (Wu *et al.*, 2014c). Thus, during SV regeneration via ADBE, multiple protein sorting steps may be required to ensure that the SVs harbor the proper compositions of lipids and proteins, thereby endowing specific release probabilities in relation to other modes of endocytosis (Cheung *et al.*, 2010; Hoopmann *et al.*, 2010; Nicholson-Fish *et al.*, 2015; Silm *et al.*, 2019). The mechanism by which protein sorting and membrane retrieval are coordinated in this process remains to be explored.

Here, we show that, upon intense stimulation, PI(4,5)P₂ is compartmentalized into microdomains at periaxial zones in the synaptic boutons of *Drosophila* larval neuromuscular junctions (NMJs). Blockade of PI(4,5)P₂ microdomain formation diminishes ADBE and SV reformation from the bulk endosome. Increased intracellular Ca²⁺ and SV exocytosis are prerequisites for initiating ADBE (Morton *et al.*, 2015; Wu and Wu, 2007). We have previously shown that Flower (Fwe), a SV-associated Ca²⁺ channel, regulates both CME and ADBE, and that its channel activity is strongly activated upon intense stimulation to elicit ADBE (Yao *et al.*, 2017). We show that Fwe initiates a positive feedback loop upon PI(4,5)P₂ increase to ensure the formation of PI(4,5)P₂ microdomains and thus trigger ADBE and subsequent SV reformation. Intriguingly, PI(4,5)P₂ also participates in retrieval of Fwe to the bulk endosome, thereby stopping membrane recycling. Hence, spatiotemporal interplays between Flower and PI(4,5)P₂ coordinate the retrieval of SV cargoes and membranes, coupling exocytosis to ADBE and subsequent SV reformation.

Results

Intense neuronal activity induces formation of PI(4,5)P₂ microdomains at the presynaptic periactive zone of *Drosophila* synapses

To investigate the dynamics of PI(4,5)P₂ in the presynaptic compartment, we expressed a GFP fusion protein of the pleckstrin homology (PH) domain of PLC_{δ1} (PLC_{δ1}-PH-EGFP) in synaptic boutons of *Drosophila* larval NMJs using *nSyb-GAL4*, a pan-neuronal driver. PLC_{δ1}-PH-EGFP binds to PI(4,5)P₂ with high affinity and is widely used to label subcellular compartments in which PI(4,5)P₂ is enriched (Chen et al., 2014; Khuong et al., 2010). We delivered 20 Hz stimuli for three minutes to synaptic boutons in a 2 mM extracellular Ca²⁺ solution and performed live imaging in the third minute. Consecutive snapshot images were taken before stimulation, during the third minute of stimulation, and after stimulation. As shown in Figure 1a–b, we observed a very subtle increase in PLC_{δ1}-PH-EGFP fluorescence in individual boutons (white arrows), similar to findings of a previous study (Verstreken et al., 2009). However, when we raised the stimulus intensity to 40 Hz, we recorded a robust increase in fluorescence relative to a GFP fusion protein of the plasma membrane-integrated mCD8 domain (*UAS-mCD8-GFP*). Fluorescence signals rapidly returned to basal levels within tens of seconds when the stimuli were removed. We have previously documented that treatment with 40 Hz electric pulses or 90 mM high KCl solution can cause comparable stimulation intensities in *Drosophila* NMJ boutons (Yao et al., 2017). High K⁺ treatment also increased the fluorescence signal of PLC_{δ1}-PH-EGFP. No increase in the presynaptic protein level of PLC_{δ1}-PH-EGFP was found under this condition (Figure 1—figure supplement 1a–b), arguing that this stimulation does not induce protein synthesis. These results suggest that, in response to intense stimulation, PLC_{δ1}-PH-EGFP is redistributed and concentrated to PI(4,5)P₂-enriched subdomains of the plasma membrane, thereby enhancing the overall fluorescence.

To characterize the subcellular distribution of the stimulus-dependent PI(4,5)P₂ induction, we conducted a chemical fixation protocol whereby the NMJ boutons were fixed at rest or immediately after high K⁺ stimulation and then immunostained for PLC_{δ1}-PH-EGFP using an α -GFP antibody to enhance the signal for high-resolution microscopic imaging. Confocal images revealed that, for neurons at rest, native PLC_{δ1}-PH-EGFP fluorescence was weakly detected on the presynaptic plasma membrane labeled by α -Hrp staining, with some additional fluorescent signal being dispersed in the cytosol (Figure 1—figure supplement 1c). We then elevated PI(4,5)P₂ on the plasma membrane by removing a copy of *synaptotjanin* (*synj*), which encodes the major neuronal PI(4,5)P₂ phosphatase (Tsujiyama et al., 2001; Verstreken et al., 2003). Consistent with previous studies (Chen et al., 2014; Verstreken et al., 2009), this reduction in *Synj* levels enhanced PLC_{δ1}-PH-EGFP fluorescence (Figure 1—figure supplement 1c–d). In this context, we did not observe a significant change in protein expression of PLC_{δ1}-PH-EGFP in the presynaptic compartment (Figure 1—figure supplement 1e–f). By using α -GFP immunostaining, these PLC_{δ1}-PH-EGFP signals could be faithfully amplified (Figure 1—figure supplement 1c–d). Therefore, this immunostaining approach was subsequently used to monitor presynaptic PI(4,5)P₂ levels.

Next, we stimulated the boutons expressing PLC_{δ1}-PH-EGFP with 90 mM K⁺ and 2 mM Ca²⁺ for 10 min. Similar to our live-imaging results, PLC_{δ1}-PH-EGFP signals were significantly increased on the presynaptic plasma membrane (Figure 1—figure supplement 1g–h). In particular, we observed high-level induction of PLC_{δ1}-PH-EGFP puncta (Figure 1c–d). To assess the possibility that chemical fixation may have altered membrane properties and consequently plasma membrane PLC_{δ1}-PH-EGFP clustering upon intense stimulation, we further examined the distributions of mCD8-GFP and PLC_{δ1}-PHS39R-EGFP, a PI(4,5)P₂-binding mutant (Khuong et al., 2010; Verstreken et al., 2009). There was no obvious change in the plasma membrane pattern of mCD8-GFP in fixed boutons stimulated with high K⁺ (Figure 1—figure supplement 2a–b). Unlike PLC_{δ1}-PH-EGFP, PLC_{δ1}-PHS39R-EGFP was found mainly in the cytosol at rest. After intense stimulation, immunostaining signals of PLC_{δ1}-PHS39R-EGFP did not accumulate on the plasma membrane (Figure 1—figure supplement 2c–d) and were not increased within the boutons (Figure 1—figure supplement 2e). Thus, clustering of PLC_{δ1}-PH-EGFP on the plasma membrane upon stimulation results from an increase in local PI(4,5)P₂ concentration, although a potential effect of chemical fixation, if any, on PLC_{δ1}-PH-EGFP clustering cannot be excluded. To assess potential dominant-negative effects of PI(4,5)P₂ binding by PLC_{δ1}-PH-EGFP on the stimulation-induced accumulation of PI(4,5)P₂, we further examined the recruitment of the AP-2 complex by PI(4,5)P₂. Similar to PLC_{δ1}-PH-EGFP, levels of the α subunit of

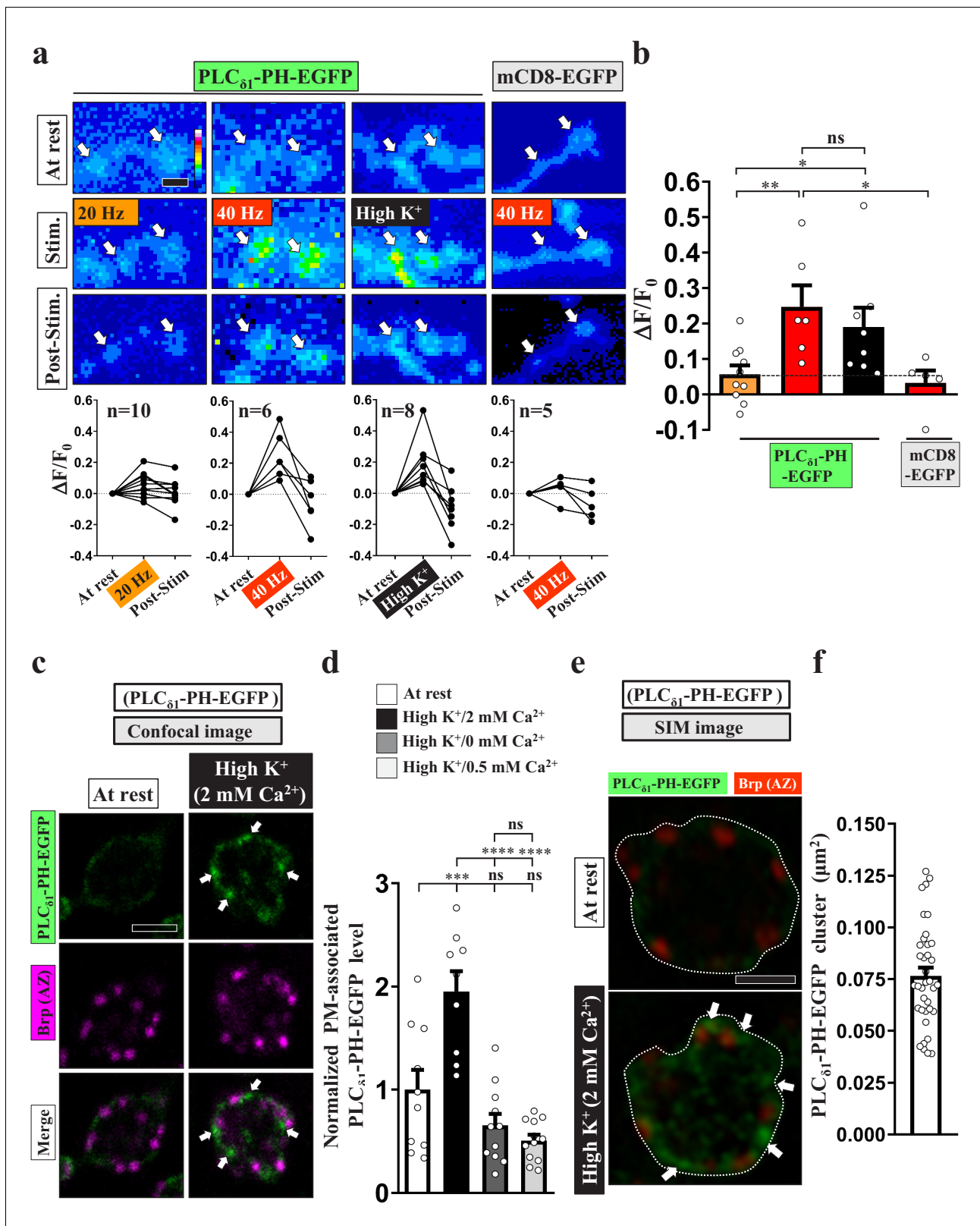


Figure 1. PI(4,5)P₂ forms microdomains at periactive zones under conditions of intense stimulation. (a–b) Increased fluorescence of PLC_{δ1}-PH-EGFP but not mCD8-GFP in NMJ boutons upon intense stimulation. (a) (Top) Live images of the boutons (arrows) expressing UAS-PLC_{δ1}-PH-EGFP or UAS-mCD8-GFP. The larvae were reared at 25°C. Electrical (20 or 40 Hz) or chemical (90 mM K⁺) stimulation was conducted in a 2 mM-Ca²⁺ solution for 3 min (electrical) or 5 min (chemical) and then rested in 0 mM Ca²⁺ and 5 mM K⁺. Snapshot images taken before stimulation, at the third (electrical) and fifth (chemical) stimulation. (b) Bar graph showing the average change in fluorescence (ΔF/F₀) of PLC_{δ1}-PH-EGFP (green) and mCD8-EGFP (grey) during stimulation. (c) Confocal images of PLC_{δ1}-PH-EGFP (green) and Brp (AZ) (magenta) at rest and High K⁺ (2 mM Ca²⁺). (d) Bar graph showing the normalized PM-associated PLC_{δ1}-PH-EGFP level at rest and during stimulation. (e) SIM images of PLC_{δ1}-PH-EGFP (green) and Brp (AZ) (red) at rest and High K⁺ (2 mM Ca²⁺). (f) Bar graph showing the PLC_{δ1}-PH-EGFP cluster area (μm²) at rest and High K⁺ (2 mM Ca²⁺). Statistical significance is indicated by asterisks (* p < 0.05, ** p < 0.01, *** p < 0.001, **** p < 0.0001, ns = not significant).

Figure 1 continued

(chemical) min of stimulation, and after stimulation. (Bottom) Traces of probe fluorescence for single boutons. The number of boutons imaged (N). (b) Quantification data for EGFP fluorescence change. The resting fluorescence level (F_0). Fluorescence change evoked by stimulation (ΔF). (c–f) PLC $_{\delta 1}$ -PH-EGFP enrichment at periaxial zones is dependent on Ca $^{2+}$ upon intense stimulation. Single-plane confocal (c) or SIM (e) images of the boutons expressing PLC $_{\delta 1}$ -PH-EGFP. The larvae were reared at 25°C. The boutons subjected to high K $^+$ /2 mM Ca $^{2+}$ (10 min stimulation of 90 mM K $^+$ /2 mM Ca $^{2+}$), high K $^+$ /0 mM Ca $^{2+}$ (10 min stimulation of 90 mM K $^+$ /0 mM Ca $^{2+}$), or high K $^+$ /0.5 mM Ca $^{2+}$ (1 min stimulation of 90 mM K $^+$ /0.5 mM Ca $^{2+}$) treatments were fixed immediately and immunostained for PLC $_{\delta 1}$ -PH-EGFP (green) and Bruchpilot (Brp) [an active zone scaffold protein; magenta (c), red (e)]. The PLC $_{\delta 1}$ -PH-EGFP-enriched puncta (Arrows). (d) Quantification data for PLC $_{\delta 1}$ -PH-EGFP staining intensities, normalized to the value of the resting condition. (f) Average area of PLC $_{\delta 1}$ -PH-EGFP clusters in individual boutons, as measured by SIM. Individual data values are shown in graphs. p values: ns, not significant; *p<0.05; **p<0.01; ***p<0.001; ****p<0.0001. Mean \pm SEM. Scale bar: 1 μ m (e), 2 μ m (a, c). Statistics: one-way ANOVA with Tukey's post hoc test (b, d).

The online version of this article includes the following source data and figure supplement(s) for figure 1:

Source data 1. Source data for **Figure 1**.

Figure supplement 1. The change in PLC $_{\delta 1}$ -PH-EGFP fluorescence is responsible for an increase in the PI(4,5)P $_2$ level.

Figure supplement 1—source data 1. Source data for **Figure 1—figure supplement 1**.

Figure supplement 2. The distribution of mCD8-EGFP and PLC $_{\delta 1}$ -PHS39R-EGFP remains unchanged upon intense stimulation.

Figure supplement 2—source data 1. Source data for **Figure 1—figure supplement 2**.

Figure supplement 3. PI(4,5)P $_2$ is increased at the periaxial zone upon intense stimulation.

Figure supplement 3—source data 1. Source data for **Figure 1—figure supplement 3**.

the AP-2 complex (AP-2 α) were also increased on the plasma membrane upon high K $^+$ stimulation (**Figure 1—figure supplement 3a–b**). Together, these data indicate that intense stimulation can promote the formation of PI(4,5)P $_2$ microdomains.

We noted that the induced PI(4,5)P $_2$ microdomains were primarily sited at periaxial zones marked by activity-dependent localization of Eps15 (**Figure 1c**; **Figure 1—figure supplement 3c**; **Koh et al., 2007**; **Winther et al., 2013**). Periaxial zones are known hot-spots for ADBE (**Chanaday et al., 2019**; **Kononenko and Haucke, 2015**; **Wu et al., 2014a**). By using structured illumination microscopy (SIM), we estimated that the average size of these PI(4,5)P $_2$ microdomains formed after stimulation is \sim 300 nm in diameter (**Figure 1e–f**) ($0.07655 \pm 0.004 \mu\text{m}^2$, mean \pm S.E.M., $n = 37$ boutons).

Next, to determine the Ca $^{2+}$ dependence of the PI(4,5)P $_2$ microdomains, we stimulated the boutons in a solution of 90 mM K $^+$ and 0 mM Ca $^{2+}$, which resulted in failure to induce PI(4,5)P $_2$ microdomain formation (**Figure 1d**). We obtained a similar result using 1 min stimulation of 90 mM K $^+$ and 0.5 mM Ca $^{2+}$ (**Figure 1d**), which was previously shown to primarily elicit CME but not ADBE (**Yao et al., 2017**). Hence, these results suggest that intense stimulation can elicit Ca $^{2+}$ -driven compartmentalization of PI(4,5)P $_2$ at the periaxial zone in synaptic boutons of *Drosophila* NMJs.

PI(4,5)P $_2$ microdomains are involved in ADBE initiation and SV reformation from bulk endosomes

Next, we investigated the function of PI(4,5)P $_2$ microdomains in ADBE. High K $^+$ treatment is widely used to trigger ADBE in a broad range of synapses (**Akbergenova and Bykhovskaia, 2009**; **Clayton et al., 2008**; **Jin et al., 2019**; **Stevens et al., 2012**; **Vijaykrishnan et al., 2009**; **Wu and Wu, 2007**; **Wu et al., 2014c**). To measure ADBE, we induced ADBE with 90 mM K $^+$ and 2 mM Ca $^{2+}$ for 10 min and then conducted transmission electron microscopy (TEM). ADBE was evoked in wild-type control boutons under these conditions and generated the formation of bulk endosomes (red asterisks, defined as >80 nm in diameter) (**Figure 2c–d**). To suppress the function of PI(4,5)P $_2$, we expressed PLC $_{\delta 1}$ -PH-EGFP, anticipating that binding of the PLC $_{\delta 1}$ -PH domain to PI(4,5)P $_2$ would restrict availability of PI(4,5)P $_2$ to its effectors and metabolic enzymes (**Figure 2a**; **Khuong et al., 2013**). By using the GAL4/UAS system, we were able to adjust expression levels of the PLC $_{\delta 1}$ -PH domain via temperature manipulation (**Brand and Perrimon, 1993**; **D'Avino and Thummel, 1999**; **Wilder, 2000**). When we neuronally expressed PLC $_{\delta 1}$ -PH-EGFP using *nSyb*-GAL4 and grew larvae at 25°C, we found that mild expression of PLC $_{\delta 1}$ -PH-EGFP had a mild inhibitory effect on ADBE induction relative to wild-type control boutons (**Figure 2c–d**). In contrast, when larvae were grown at 29°C to effect a two-fold increase in PLC $_{\delta 1}$ -PH-EGFP expression (**Figure 2—figure supplement 1a–b**),

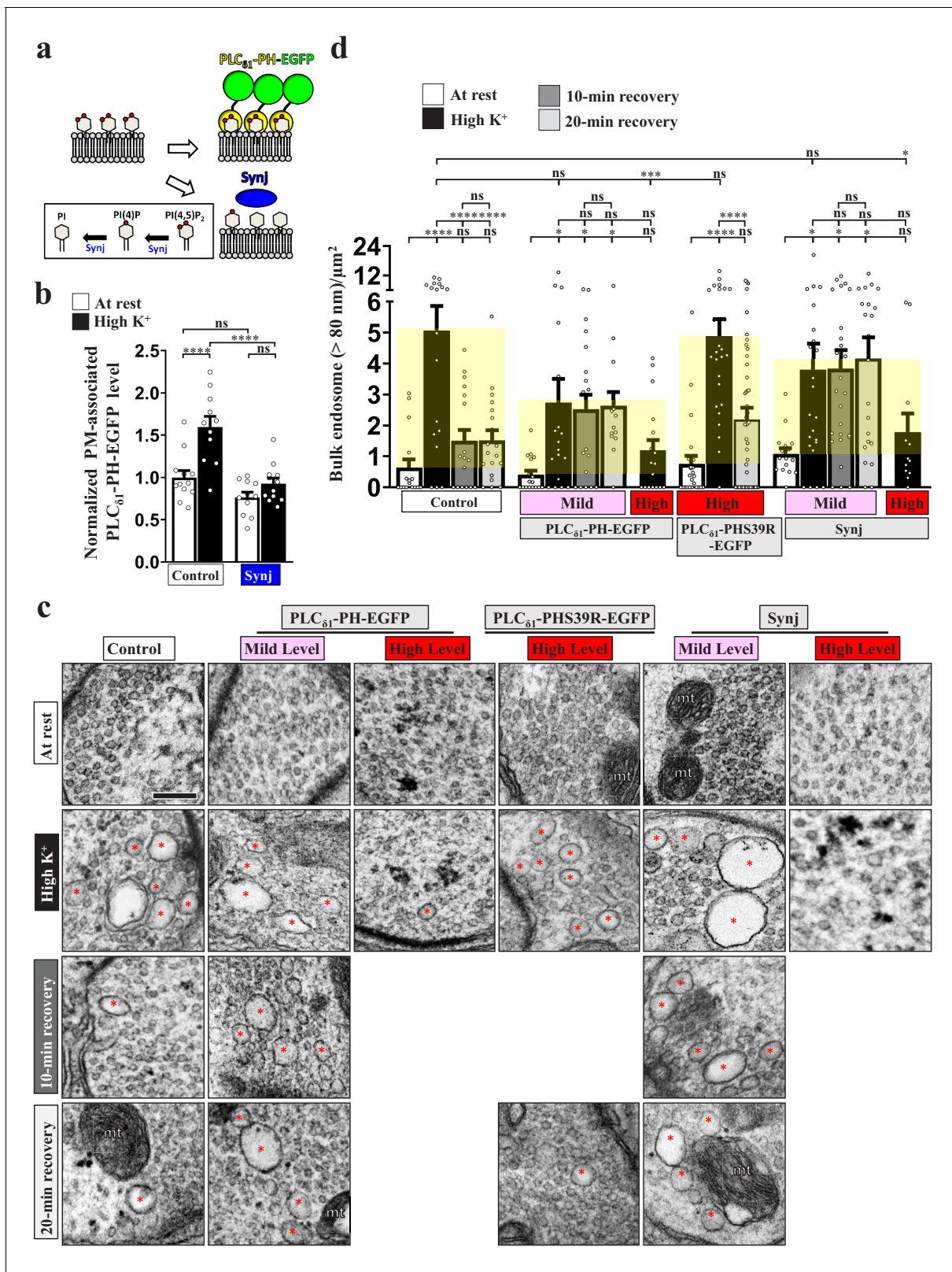


Figure 2. PI(4,5)P₂ microdomains drive ADBE and SV reformation from bulk endosomes. Reducing PI(4,5)P₂ availability suppresses ADBE and subsequent SV reformation. (a) A schematic for PI(4,5)P₂ suppression by PLC_{δ1}-PH-EGFP or Synj expression. (b) Expression of Synj reduced presynaptic plasma membrane PI(4,5)P₂ upon high K⁺ treatment. The boutons co-expressing UAS-PLC_{δ1}-PH-EGFP with UAS-RFP (control) or UAS-synj using *nSyb-GAL4* were reared at 25°C and subjected to resting condition (10 min incubation of 5 mM K⁺/0 mM Ca²⁺) or high K⁺ stimulation (10 min stimulation of Figure 2 continued on next page

Figure 2 continued

90 mM K⁺/2 mM Ca²⁺), followed by α -GFP immunostaining. Single-plane confocal images of the boutons are shown in **Figure 2—figure supplement 1c**. Quantification data for PLC δ_1 -PH-EGFP staining intensity are shown, normalized to the value of the resting condition of controls. (c) TEM images of the boutons of controls (*nSyb-GAL4/+* at 29°C), mild PLC δ_1 -PH-EGFP expression (*nSyb-GAL4/UAS-PLC δ_1 -PH-EGFP* at 25°C), high PLC δ_1 -PH-EGFP expression (*nSyb-GAL4/UAS-PLC δ_1 -PH-EGFP* at 29°C), high PLC δ_1 -PHS39R-EGFP expression (*nSyb-GAL4/UAS-PLC δ_1 -PHS39R-EGFP* at 29°C), mild Synj expression (*nSyb-GAL4/UAS-synj* at 25°C), or high Synj expression (*nSyb-GAL4/UAS-synj* at 29°C). At rest (10 min incubation of 5 mM K⁺/0 mM Ca²⁺). High K⁺ (10 min stimulation of 90 mM K⁺/2 mM Ca²⁺). 10 min recovery (10 min stimulation of 90 mM K⁺/2 mM Ca²⁺, followed by 10 min incubation of 5 mM K⁺/0 mM Ca²⁺). 20 min recovery (10 min stimulation of 90 mM K⁺/2 mM Ca²⁺, followed by 20 min incubation of 5 mM K⁺/0 mM Ca²⁺). Bulk endosomes (>80 nm in diameter, red asterisks). Mitochondria (mt). Quantification data for total number of bulk endosomes per bouton area (d). Individual data values are shown in graphs. p values: ns, not significant; *p<0.05; **p<0.01; ***p<0.001; ****p<0.0001. Mean \pm SEM. Scale bar: 500 nm. Statistics: one-way ANOVA with Tukey's post hoc test.

The online version of this article includes the following source data and figure supplement(s) for figure 2:

Source data 1. Source data for **Figure 2**.

Figure supplement 1. Blockade of the PI(4,5)P₂ microdomains by expressing PLC δ_1 -PH-EGFP and Synj.

Figure supplement 1—source data 1. Source data for **Figure 2—figure supplement 1**.

Figure supplement 2. Blockade of the PI(4,5)P₂ microdomains abolishes SV reformation from the bulk endosome.

Figure supplement 2—source data 1. Source data for **Figure 2—figure supplement 2**.

ADBE was almost completely abolished (**Figure 2c–d**). However, when larvae expressing PLC δ_1 -PHS39R-EGFP were grown at 29°C, ADBE was not suppressed by the mutant protein (**Figure 2c–d**).

Synj comprises a central 5-phosphatase domain that specifically dephosphorylates the 5' position of PI(4,5)P₂ to produce PI(4)P (*McPherson et al., 1996; Woscholski et al., 1997*). In addition, an N-terminal Sac1 domain converts several phosphatidylinositides—including PI(3,5)P₂, PI(3)P, and PI(4)P—to PI (**Figure 2a; Guo et al., 1999). Indeed, overexpression of Synj reduced the formation of the PI(4,5)P₂ microdomains induced by high K⁺ (**Figure 2b; Figure 2—figure supplement 1c**). Importantly, overexpression of Synj resulted in dosage-dependent inhibition of ADBE (**Figure 2c–d**), similar to the effect of increasing levels of the PLC δ_1 -PH domain. Together, these data suggest that the PI(4,5)P₂ microdomains initiate ADBE to control SV membrane retrieval upon intense stimulation.**

SVs regenerate from bulk endosomes within minutes of their formation (*Cheung and Cousin, 2012; Glyvuk et al., 2010; Kononenko et al., 2014; Stevens et al., 2012; Wu et al., 2014c*). Using an approach employed previously (*Stevens et al., 2012*), we treated the boutons with high K⁺ followed by an incubation in 5 mM K⁺ and 0 mM Ca²⁺ solution for 10 or 20 min, allowing the SVs to reform from the bulk endosomes. In controls (*nSyb-GAL4*), the number and area of the induced bulk endosomes reverted to almost basal levels within 10 min (**Figure 2c–d; Figure 2—figure supplement 2**), demonstrating proper SV reformation. Interestingly, upon expression of low levels of PLC δ_1 -PH-EGFP, the induced bulk endosomes remained after 10 min and 20 min recovery periods, yet ADBE was only partially impaired (**Figure 2c–d; Figure 2—figure supplement 2**). In contrast, SV reformation actively occurred in the boutons expressing high levels of PLC δ_1 -PHS39R-EGFP (**Figure 2c–d; Figure 2—figure supplement 2**). Furthermore, we observed a loss of SV reformation ability upon mild overexpression of Synj (**Figure 2c–d; Figure 2—figure supplement 2**). Hence, the formation of PI(4,5)P₂ microdomains is essential for both ADBE and SV reformation from the bulk endosome, with the latter event being elicited by relatively high levels of PI(4,5)P₂. Note that perturbation of PI(4,5)P₂ microdomain formation did not cause SV accumulation on the bulk endosome during recovery periods, indicating that PI(4,5)P₂ microdomains may play an early role in SV reformation from bulk endosomes.

PI(4,5)P₂ microdomains are established via a positive feedback loop of Fwe and PI(4,5)P₂

We have previously shown that the SV-associated Ca²⁺ channel Flower (Fwe) elevates presynaptic Ca²⁺ levels in response to strong stimuli to trigger ADBE (*Yao et al., 2009; Yao et al., 2017*). Given the Ca²⁺ dependence of PI(4,5)P₂ microdomains (**Figure 1d**), we hypothesized that exocytosis evoked by intense stimulation promotes Fwe clustering at periaxial zones, where it may provide the Ca²⁺ influx to induce PI(4,5)P₂ microdomain formation. To test this hypothesis, we first conducted a proximity ligation assay (PLA) (*Söderberg et al., 2008*) to investigate if there is a close association between Fwe and PI(4,5)P₂ in response to stimulation. In our PLA (**Figure 3a**), UAS-Flag-

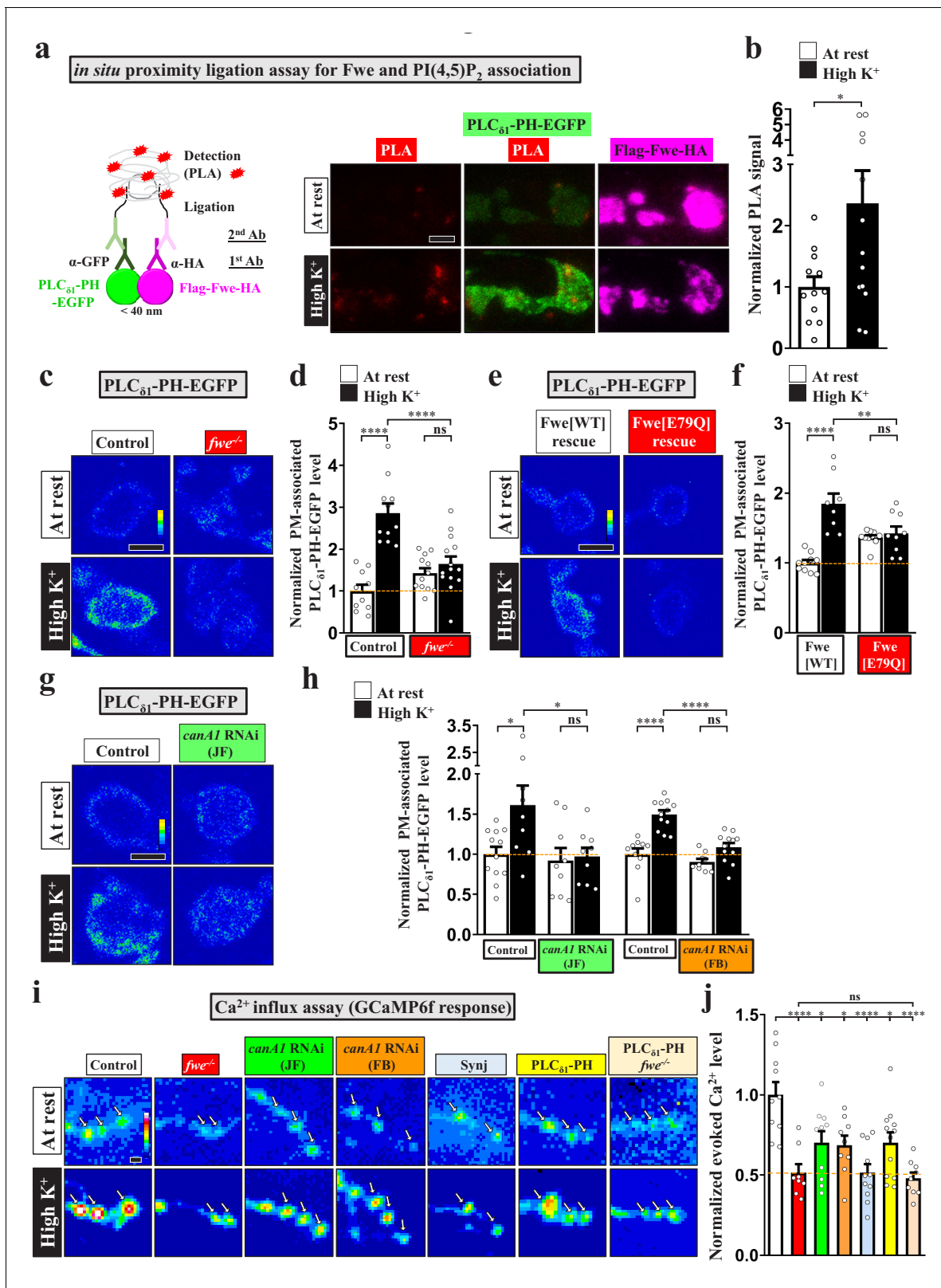


Figure 3. Fwe and PI(4,5)P₂ form a positive feedback loop to establish PI(4,5)P₂ microdomains. (a–b) Fwe and PLC_{δ1}-PH-EGFP interact upon intense stimulation. (a) (Left) A schematic for PLA. (Right) Z-projected confocal images of *fwe* mutant boutons co-expressing Flag-Fwe-HA and PLC_{δ1}-PH-EGFP (*nSyb-GAL4/UAS-Flag-fwe-HA/UAS-PLC_{δ1}-PH-EGFP* in *fwe*^{DB25/DB56} at 25°C). After resting condition or high K⁺ stimulation, the boutons were subjected to PLA. α-GFP and α-HA stained for PLC_{δ1}-PH-EGFP (green) and Flag-Fwe-HA (magenta), respectively. PLA signals (red). (b) Quantification data for PLA

Figure 3 continued on next page

Figure 3 continued

signal intensities, normalized to the value of the resting condition. (c–f) Loss of Fwe or its Ca^{2+} channel activity perturbs $\text{PI}(4,5)\text{P}_2$ microdomain formation. (c and e). (c) Single-plane confocal images of the boutons neuronally expressing $\text{UAS-PLC}_{\delta 1}\text{-PH-EGFP}$ in $\text{fwe}^{\text{DB25/+}}$ (control) or $\text{fwe}^{\text{DB25/DB56}}$ at 25°C. The boutons were subjected to resting condition or high K^+ stimulation, followed by $\alpha\text{-GFP}$ immunostaining. Quantification data for $\text{PLC}_{\delta 1}\text{-PH-EGFP}$ staining intensity are shown, normalized to the value of the resting condition of controls (d). (e) Single-plane confocal images of the boutons neuronally expressing $\text{lexAop2-PLC}_{\delta 1}\text{-PH-EGFP}$ using vglut-lexA in wild-type Fwe rescue boutons ($\text{vglut-lexA/lexAop2-PLC}_{\delta 1}\text{-PH-EGFP}$, $n\text{Syb(w)-GAL4/UAS-flag-fwe-RB-HA}$ in $\text{fwe}^{\text{DB25/fweDB56}}$ at 25°C), or FweE79Q rescue boutons ($\text{vglut-lexA/lexAop2-PLC}_{\delta 1}\text{-PH-EGFP}$, $n\text{Syb(w)-GAL4/UAS-flag-fweE79Q-RB-HA}$ in $\text{fwe}^{\text{DB25/fweDB56}}$ at 25°C). When the weak $n\text{Syb(w)-GAL4}$ driver drove low expression of UAS-fwe transgenes, this binary system ($\text{vglut-lexA/lexAop2-PLC}_{\delta 1}\text{-PH-EGFP}$) was used to produce detectable levels of $\text{PLC}_{\delta 1}\text{-PH-EGFP}$ in boutons. Quantification data for $\text{PLC}_{\delta 1}\text{-PH-EGFP}$ staining intensity are shown, normalized to the value of the resting condition of Fwe-rescued boutons (f). (g–h) canA1 RNAi knockdown impairs $\text{PI}(4,5)\text{P}_2$ microdomain formation. Single-plane confocal images of the boutons co-expressing $\text{UAS-PLC}_{\delta 1}\text{-PH-EGFP}$ with UAS-RFP (control), UAS-canA1-RNAi (TRiP.JF01871), or UAS-canA1-RNAi (FB4) using $n\text{Syb-GAL4}$. The larvae were reared at 25°C. After resting condition or high K^+ stimulation, the boutons were stained with $\alpha\text{-GFP}$. (h) Quantification data for $\text{PLC}_{\delta 1}\text{-PH-EGFP}$ staining intensities, normalized to the value of the resting condition of controls. (i–j) Blockade of the $\text{PI}(4,5)\text{P}_2$ microdomains attenuates Fwe Ca^{2+} conductance. (i) Snapshot Ca^{2+} images of the boutons (arrows) expressing lexAop2-GCaMP6f using vglut-lexA . The larvae of control (w^{1118}), fwe mutant ($\text{fwe}^{\text{DB25/DB56}}$), canA1 RNAi (JF) ($n\text{Syb-GAL4/UAS-canA1-RNAi}$ (TRiP.JF01871)), canA1 RNAi (FB) ($n\text{Syb-GAL4/UAS-canA1-RNAi}$ (FB4)), Synj overexpression ($n\text{Syb-GAL4/UAS-synj}$), $\text{PLC}_{\delta 1}\text{-PH-APEX2-HA}$ expression ($\text{vglut-lexA/LexAop2-PLC}_{\delta 1}\text{-PH-APEX2-HA}$), or fwe mutant expressing $\text{PLC}_{\delta 1}\text{-PH-APEX2-HA}$ ($\text{vglut-lexA/LexAop2-PLC}_{\delta 1}\text{-PH-APEX2-HA}$ in $\text{fwe}^{\text{DB25/DB56}}$) were reared at 25°C. Imaging was taken in the fifth minute for one minute after high K^+ (2 mM Ca^{2+}) stimulation. (j) Quantification data for evoked Ca^{2+} level, normalized to the value of controls. Evoked Ca^{2+} levels are shown as the increase in GCaMP6f fluorescence under high K^+ stimulation. Individual data values are shown in graphs. p values: ns, not significant; * $p < 0.05$; ** $p < 0.01$; **** $p < 0.0001$. Mean \pm SEM. Scale bar: 2 μm . Statistics: Student t-test (b). One-way ANOVA with Tukey's post hoc test (d, f, h, j).

The online version of this article includes the following source data for figure 3:

Source data 1. Source data for **Figure 3**.

Fwe-HA was expressed in a *fwe* mutant background to replace endogenous Fwe protein with a tagged protein, and expression of $\text{UAS-PLC}_{\delta 1}\text{-PH-EGFP}$ reported the localization of $\text{PI}(4,5)\text{P}_2$. Primary antibodies against the HA tag and EGFP protein were used to detect interactions between Flag-Fwe-HA and $\text{PLC}_{\delta 1}\text{-PH-EGFP}$. The PLA signal was low in resting boutons, whereas high K^+ treatment significantly increased PLA signal intensity (**Figure 3a–b**). Therefore, these results suggest that Fwe and $\text{PI}(4,5)\text{P}_2$ are closely colocalized when intense stimulation triggers $\text{PI}(4,5)\text{P}_2$ microdomain formation.

Next, we investigated the effect of loss of Fwe on $\text{PI}(4,5)\text{P}_2$ microdomain formation. Basal levels of $\text{PI}(4,5)\text{P}_2$ were not affected in the *fwe* mutant relative to control (**Figure 3c–d**). However, intense stimulation failed to elicit $\text{PI}(4,5)\text{P}_2$ microdomain formation in the *fwe* mutant (**Figure 3c–d**), revealing a crucial role for Fwe in this process. To determine if the Ca^{2+} channel activity of Fwe is responsible for this activity, we conducted rescue experiments based on our previous report in which *fwe* mutant boutons exhibited expression of the wild-type Fwe transgene or the FweE79Q mutant transgene that has reduced Ca^{2+} conductance (Yao et al., 2017). We found that the wild-type Fwe transgene promoted $\text{PI}(4,5)\text{P}_2$ microdomain formation, whereas the FweE79Q mutant transgene lost that ability (**Figure 3e–f**). Thus, Fwe triggers the formation of $\text{PI}(4,5)\text{P}_2$ microdomains in a Ca^{2+} channel-dependent manner.

Calmodulin and Calcineurin are thought to be the Ca^{2+} sensors for ADBE (Evans and Cousin, 2007; Jin et al., 2019; Marks and McMahon, 1998; Sun et al., 2010; Wu et al., 2009; Wu et al., 2014b). The Calcineurin complex dephosphorylates $\text{PI}(4,5)\text{P}_2$ metabolic enzymes, including Synj and Phosphatidylinositol 4-phosphate 5-kinase γ ($\text{PIP}2\text{K}\gamma$) (Cousin and Robinson, 2001; Lee et al., 2005; Lee et al., 2004; van den Bout and Divecha, 2009). *Drosophila* possesses three isoforms of the catalytic subunit of Calcineurin, i.e., CanA1, CanA-14F, and Pp2B-14D. CanA1 regulates development of *Drosophila* NMJ boutons (Wong et al., 2014). Therefore, we knocked down *canA1* in neurons by using two independent UAS-canA1-RNAi constructs, UAS-canA1-RNAi (JF01871) (Wong et al., 2014) and UAS-canA1-RNAi (FB4) (Dijkers and O'Farrell, 2007). Similar to the effect of loss of Fwe, reducing CanA1 levels via expression of either RNAi construct greatly suppressed the formation of $\text{PI}(4,5)\text{P}_2$ microdomains compared to the control (**Figure 3g–h**), indicating that Calcineurin mediates the Ca^{2+} influx conducted by Fwe to induce $\text{PI}(4,5)\text{P}_2$ microdomains.

Our previous Ca^{2+} imaging data showed that intense stimulation activates Fwe to increase pre-synaptic Ca^{2+} concentrations (Yao et al., 2017). We measured intracellular Ca^{2+} levels with the Ca^{2+} indicator GCaMP6f (Chen et al., 2013), and found that whereas control boutons exhibited a robust

increase in intracellular Ca^{2+} upon high K^+ stimulation, *fwe* mutant boutons exhibit an impaired Ca^{2+} response (**Figure 3i–j**). Unexpectedly, *canA1* knockdown also elicited the same deficient Ca^{2+} response (**Figure 3i–j**). Similar suppressive effects were obtained upon overexpressing Synj or the $\text{PLC}_{\delta 1}$ -PH domain (**Figure 3i–j**). Hence, Calcineurin activation may increase $\text{PI}(4,5)\text{P}_2$ activity, which may in turn promote the Ca^{2+} channel activity of Fwe to further increase intracellular Ca^{2+} levels. To investigate the potential for such feedback regulation, we expressed the $\text{PLC}_{\delta 1}$ -PH domain in a loss of Fwe background. Expression of the $\text{PLC}_{\delta 1}$ -PH domain did not rescue the low Ca^{2+} concentration caused by the *fwe* mutation (**Figure 3i–j**), showing that the Ca^{2+} suppression exerted by the $\text{PLC}_{\delta 1}$ -PH domain indeed depends on Fwe. These findings support that a positive feedback loop involving Fwe and $\text{PI}(4,5)\text{P}_2$ is responsible for the formation of $\text{PI}(4,5)\text{P}_2$ microdomains.

$\text{PI}(4,5)\text{P}_2$ gates *fwe*

A well-known function of $\text{PI}(4,5)\text{P}_2$ is to modulate ion channel activity through its electrostatic binding to clustered positively-charged amino acids adjacent to the transmembrane domains of ion channels (Hille et al., 2015; Suh and Hille, 2008). Through protein alignment analysis, we found tandem positively-charged amino acids, including lysine (K) and arginine (R), in the intracellular juxta-transmembrane regions of Fwe. These residues are evolutionarily conserved in mice and humans (**Figure 4a**), whereas other cytosolic residues show poor conservation. This feature inspired us to test the potential impact of $\text{PI}(4,5)\text{P}_2$ on the channel function of Fwe. To determine direct interaction between Fwe and $\text{PI}(4,5)\text{P}_2$, we conducted a nanoluciferase (Nluc)-based bioluminescence resonance energy transfer (BRET) assay (Cabanos et al., 2017). In our BRET assay (**Figure 4a**), upon ion channel binding of BODIPY-TMR-conjugated $\text{PI}(4,5)\text{P}_2$, illumination of Nluc-fused ion channels wrapped in detergent-formed micelles can excite BODIPY-TMR-conjugated $\text{PI}(4,5)\text{P}_2$ to emit a BRET signal. As shown in **Figure 4b**, we reconstituted the micelles containing purified Nluc-Fwe-1D4 fusion proteins and, after adding BODIPY-TMR- $\text{PI}(4,5)\text{P}_2$ and furimazine (a Nluc substrate), we observed a remarkable increase in BRET signal. Excess cold $\text{PI}(4,5)\text{P}_2$ reduced the signal to ~50% of the BRET signals by competing for the $\text{PI}(4,5)\text{P}_2$ binding sites in Fwe, suggesting direct $\text{PI}(4,5)\text{P}_2$ binding to Fwe. To assess the involvement of the positively-charged amino acids of Fwe in $\text{PI}(4,5)\text{P}_2$ binding, we mutated all of the clustered positively-charged amino acids to non-charged alanine to eliminate the electrostatic interactions. Residue substitution resulted in a significant reduction in BRET signal, comparable to the competitive effect attributable to provision of excess cold $\text{PI}(4,5)\text{P}_2$. Therefore, the majority of the $\text{PI}(4,5)\text{P}_2$ binding activity of Fwe is mediated by these positively-charged amino acids. Specifically, alanine substitution of residues in both the middle (K95, K100, R105) and C-terminal (K146, K147, R150) regions of Fwe reduced $\text{PI}(4,5)\text{P}_2$ -specific binding (**Figure 4b–c**). Moreover, when N-terminal residues (K29, R33) of Fwe were further substituted with alanines, binding of $\text{PI}(4,5)\text{P}_2$ was also reduced (**Figure 4b–c**). Hence, these in vitro assays reveal that Fwe directly binds $\text{PI}(4,5)\text{P}_2$ through multiple regions.

To directly test how $\text{PI}(4,5)\text{P}_2$ affects Flower Ca^{2+} channel function, we generated UAS transgenes for the Fwe variants in which all or subsets of positively-charged amino acids were mutated to alanine and performed a mutant rescue experiment using *nSyb-GAL4*. Mutations of all nine residues or only those in the middle region (K95/K100/R105) led to very low protein expression levels, preventing further study. However, alanine substitution of C-terminal residues K146/K147/R150 did not affect SV localization of Fwe or its ability to regulate presynaptic Ca^{2+} concentration and induce $\text{PI}(4,5)\text{P}_2$ microdomain formation (**Figure 4—figure supplement 1a–f**), suggesting that these residues do not play a regulatory role in Fwe channel activity. We also mutated the N-terminal residues K29/R33. The resulting K29A/R33A variant was still able to properly localize to presynaptic terminals (**Figure 4—figure supplement 2a–b**). However, upon high K^+ stimulation, the K29A/R33A variant lost that ability to maintain proper intracellular Ca^{2+} levels (**Figure 4d–e**). Moreover, that variant failed to promote $\text{PI}(4,5)\text{P}_2$ microdomain formation upon high K^+ stimulation (**Figure 4f–g**). These results reveal that the positive feedback loop involving Fwe and $\text{PI}(4,5)\text{P}_2$ relies on $\text{PI}(4,5)\text{P}_2$ -dependent gating control of Fwe.

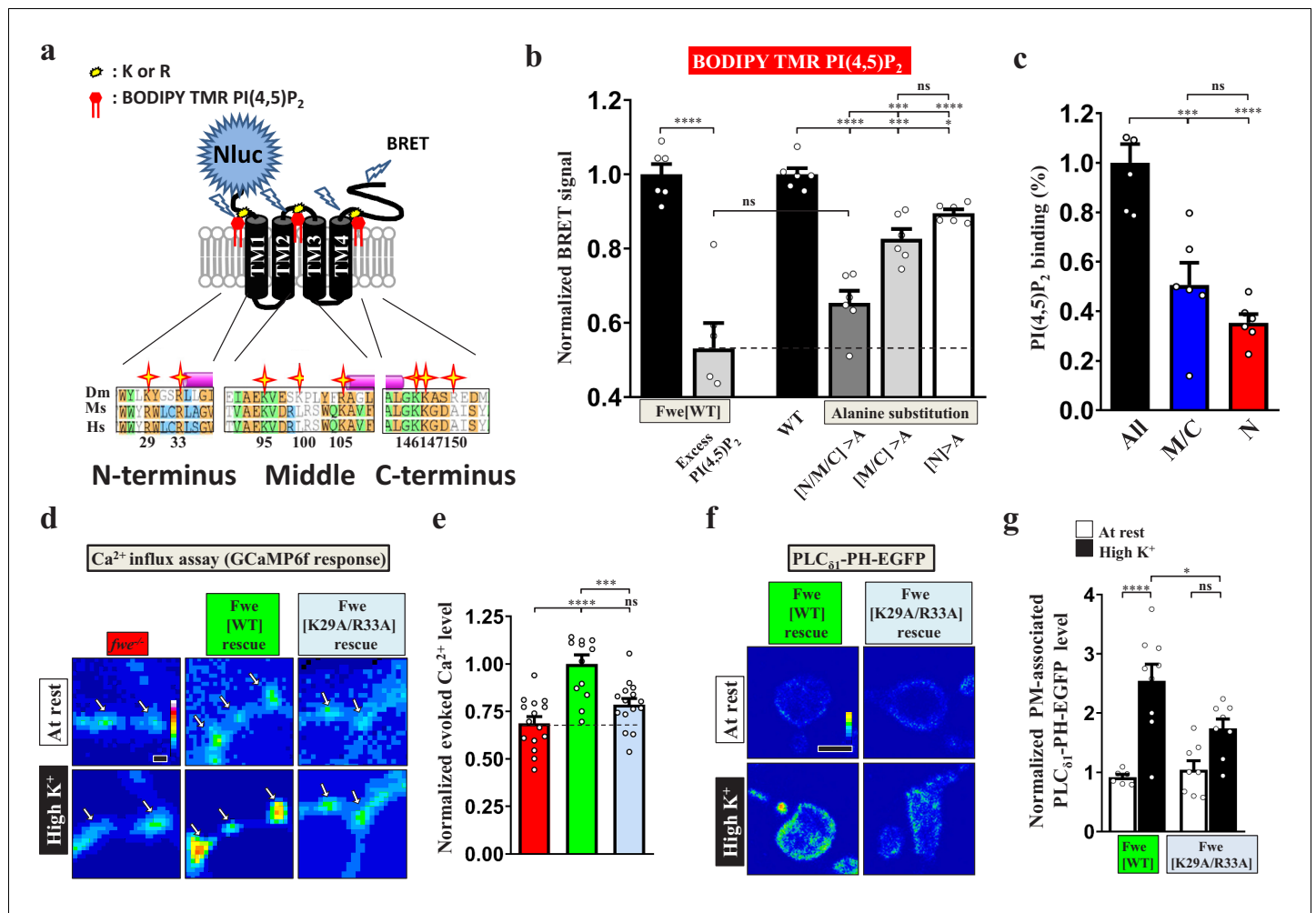


Figure 4. PI(4,5)P₂ binds to Fwe and promotes its Ca²⁺ channelling activity. (a–c) PI(4,5)P₂ binds Fwe. (a) A schematic of the Fwe structure and a BRET assay. Stars highlight conserved lysine (K) and arginine (R) in juxta-transmembrane regions: N-terminus (N), middle-domain (M), and C-terminus (C). *Drosophila melanogaster* (Dm). *Mus Musculus* (Ms). *Human Sapiens* (Hs). N-terminal fusion of Nluc to Fwe allows detection of PI(4,5)P₂ binding. A 1D4 epitope was used for protein purification. (b) Nluc-Fwe-1D4 in micelles excites BODIPY-TMR-conjugated PI(4,5)P₂ to emit BRET signal, which is decreased by competitive cold PI(4,5)P₂ (1 mM). Alanine substitution of positively-charged residues in all regions (N/M/C > A), both middle-domain and C-terminus (M/C > A), or N-terminus (N > A) reduced BRET signals. (c) Corresponding PI(4,5)P₂ binding ability was calculated by subtracting the signal values of N/M/C > A, M/C > A or N > A from that for WT. Quantification data was normalized to the signal value of all mutations (N/M/C). (d) PI(4,5)P₂ controls Fwe channel activity. Snapshot Ca²⁺ images of the boutons (arrows) expressing *lexAop2-GCaMP6f* using *vglut-lexA*. *fwe* mutant (*fwe*^{DB25/DB56}). HA-Fwe[WT]-APEX2 rescue (*nSyb-GAL4/UAS-HA-Fwe[WT]-APEX2* in *fwe*^{DB25/DB56}). HA-Fwe[K29A/R33A]-APEX2 rescue (*nSyb-GAL4/UAS-HA-Fwe[K29A/R33A]-APEX2* in *fwe*^{DB25/DB56}). The larvae were reared at 25°C. Images were taken in the fifth minute for one minute after high K⁺ stimulation. (e) Quantification data for evoked Ca²⁺ level, normalized to the value of HA-Fwe-APEX2 rescue larvae. (f) Single-plane confocal images of the boutons expressing *UAS-PLC₈₁-PH-EGFP*. The larvae were reared at 25°C. After resting conditions or high K⁺ stimulation, the boutons were stained with α -GFP. (g) Quantification data for the PLC₈₁-PH-EGFP staining intensity, normalized to the value of the resting condition of HA-Fwe-APEX2 rescue larvae. Individual data values are shown in graphs. p values: ns, not significant; *p<0.05; ***p<0.001; ****p<0.0001. Mean \pm SEM. Scale bar: 2 μ m (d, f). Statistics: Student t-test (b). One-way ANOVA with Tukey's post hoc test (b, c, e, g).

The online version of this article includes the following source data and figure supplement(s) for figure 4:

Source data 1. Source data for **Figure 4**.

Figure supplement 1. The C-terminal residues (K146/K147/R150) of Fwe are not involved in regulating Ca²⁺ channel activity.

Figure supplement 1—source data 1. Source data for **Figure 4—figure supplement 1**.

Figure supplement 2. Expression of Fwe[R29A/K33A] in boutons.

Figure supplement 2—source data 1. Source data for **Figure 4—figure supplement 2**.

Blockade of the positive feedback loop reduces ADBE and SV reformation from bulk endosomes

Next, we assessed the impact of the Fwe and PI(4,5)P₂ regulatory feedback loop on ADBE. Loss of Fwe severely impaired formation of bulk endosomes induced by ADBE under high K⁺ conditions compared to the *fwe* mutant rescue control (**Figure 5a–b**), consistent with our previous findings (Yao *et al.*, 2017). Next, we found that expression of wild-type Fwe protein or the K146A/K147A/R150A mutant variant restored proper ADBE in the *fwe* mutant background (**Figure 5a–b; Figure 4—figure supplement 1g–h**), whereas expression of the K29A/R33A variant failed to rescue ADBE deficiency (**Figure 5a–b**). Consistent with the suppressive effects caused by expression of the PLCδ1-PH domain or Synj (**Figure 2**), all of the bulk endosomes that remained in boutons lacking *fwe* could not generate new SVs during a 10 min or even 20 min recovery period (**Figure 5a–b; Figure 5—figure supplement 1**). Expression of wild-type Fwe protein but not the K29A/R33A mutant variant rescued this defect (**Figure 5a–b; Figure 5—figure supplement 1**).

Neuronal *canA1* knockdown by expressing *canA1* RNAi construct also impaired ADBE relative to the *nSyb*-GAL4 control (**Figure 5a–b**). To verify if CanA1 regulates ADBE in an Fwe-dependent manner, we overexpressed Fwe to increase the intracellular Ca²⁺ levels under *canA1* RNAi knockdown conditions. Fwe overexpression significantly reversed the ADBE defect (**Figure 5a–b**), suggesting that increasing Fwe-dependent Ca²⁺ influx can augment activation of the residual CanA1 enzymes and thus normalize downstream ADBE. Taken together with our results reported in previous sections, we propose that the positive feedback loop involving Fwe, CanA1 and PI(4,5)P₂ compartmentalizes PI(4,5)P₂ microdomains at the periaxial zone of boutons to dictate and coordinate ADBE and subsequent SV reformation.

PI(4,5)P₂ facilitates retrieval of fwe to bulk endosomes

It was reported recently that a SV protein sorting process occurs during ADBE (Kokotos *et al.*, 2018; Nicholson-Fish *et al.*, 2015). VAMP4, a v-SNARE protein, is essential for ADBE to proceed, and it is selectively retrieved by ADBE (Kokotos *et al.*, 2018; Nicholson-Fish *et al.*, 2015). Given the important role of Fwe in triggering ADBE, we wondered if Fwe is sorted to bulk endosomes during ADBE. To visualize the vesicular localization of Fwe, we rescued the *fwe* mutant by expressing a UAS transgene of the APEX2 fusion protein of Fwe (UAS-HA-Fwe-APEX2), and then conducted diaminobenzidine (DAB) labeling and TEM. By means of confocal microscopy, we observed that HA-Fwe-APEX2 immunostaining signals were properly present on the SVs marked by Syt and Csp immunostaining (**Figure 6—figure supplement 1a**). Furthermore, expression of this fusion protein was able to rescue the endocytic defects (**Figures 4 and 5**) and early animal lethality (not shown) caused by loss of *fwe*. Therefore, HA-Fwe-APEX2 is functionally equivalent to endogenous Fwe. APEX2 is an engineered peroxidase that is capable of catalyzing DAB polymerization and proximal deposition, with the DAB polymers binding electron-dense osmium to enhance electron microscopy contrast (Lam *et al.*, 2015). Whereas no DAB staining signals were observed in SVs in the Flag-Fwe-HA rescue control boutons stimulated by high K⁺ (yellow arrows, **Figure 6—figure supplement 1b'**; **Figure 6a**), the SV-based localization of HA-Fwe-APEX2 was clearly revealed by DAB staining in HA-Fwe-APEX2-rescued boutons under the resting and stimulation conditions (yellow arrows, **Figure 6—figure supplement 1c–d**). Moreover, specific DAB labeling also revealed the presynaptic plasma membrane localization of HA-Fwe-APEX2 (white arrows, **Figure 6—figure supplement 1b–c**), an outcome consistent with previous immunogold staining assays on endogenous Fwe (Yao *et al.*, 2009). Upon high K⁺ stimulation, SV and plasma membrane localizations were retained (**Figure 6—figure supplement 1d'**). Remarkably, DAB signals were apparent on all bulk endosomes (**Figure 6b–c; Figure 6—figure supplement 1d and d'**). To minimize staining variability across boutons, we compared DAB staining intensities on bulk endosomes and SVs in the same boutons. Compared to Flag-Fwe-HA rescue boutons, in HA-Fwe-APEX2 rescue boutons, the staining intensities of bulk endosomes were more abundant compared to those of the surrounding SVs (**Figure 6f**), revealing a mechanism by which Fwe is recycled to bulk endosomes after it initiates ADBE.

PI(4,5)P₂ is known to recruit adaptor protein complexes to sort SV proteins to the nascent SV during CME (Saheki and De Camilli, 2012). Next, we assessed if PI(4,5)P₂ microdomain formation may be involved in sorting of Fwe to bulk endosomes. When PI(4,5)P₂ microdomains were perturbed by Synj overexpression (**Figure 2b**), the bulk endosome localization of HA-Fwe-APEX2 was significantly

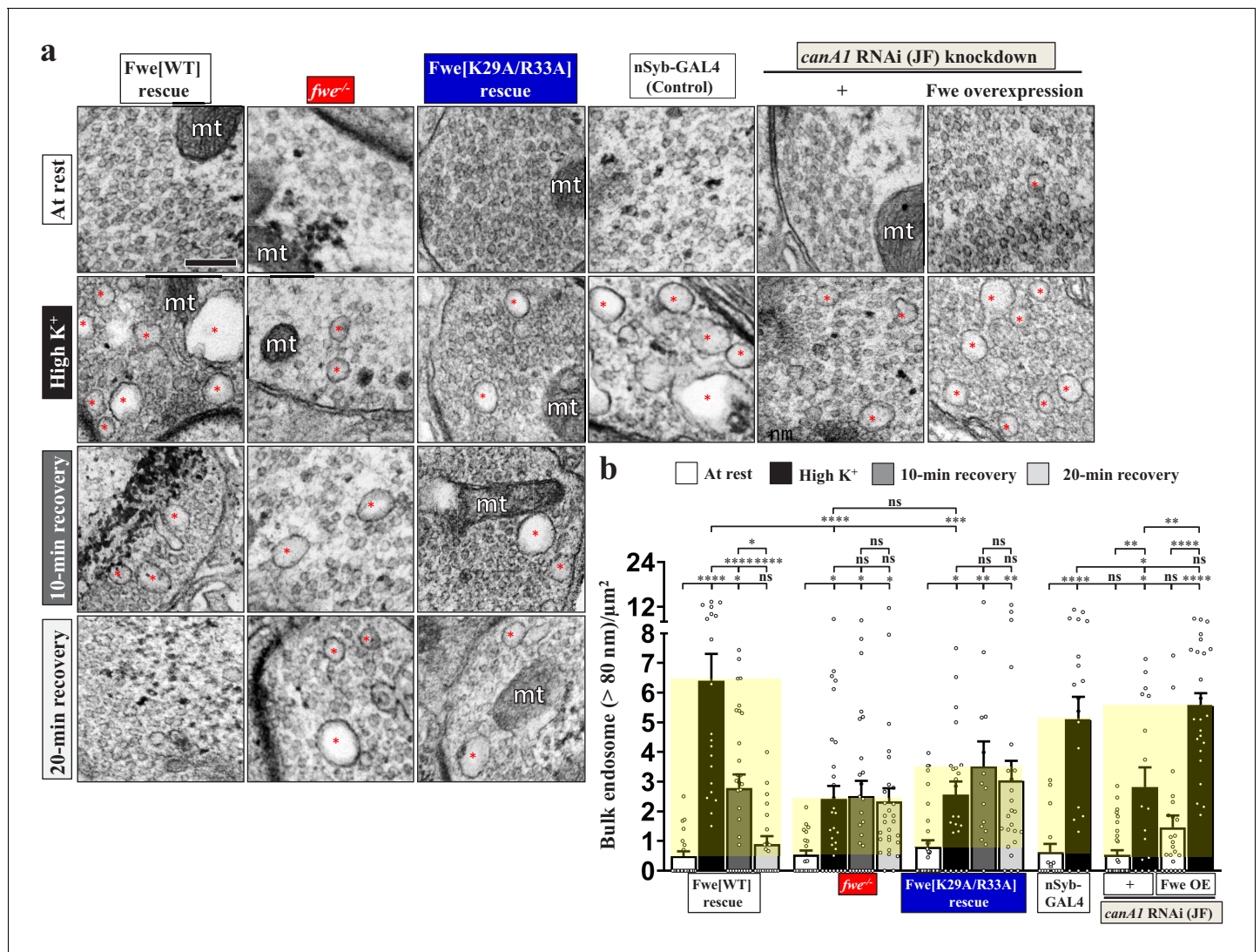


Figure 5. Perturbations of the positive feedback loop involving Fwe and PI(4,5)P₂ suppress ADBE and SV reformation from bulk endosomes. (a) TEM images of the boutons of HA-Fwe-APEX2 rescue (*nSyb-GAL4/UAS-HA-Fwe-APEX2* in *fwe^{DB25/DB56}* at 25°C), *fwe* mutant (*fwe^{DB25/DB56}* at 25°C), HA-Fwe [K29A/R33A]-APEX2 rescue (*nSyb-GAL4/UAS-HA-Fwe[K29A/R33A]-APEX2* in *fwe^{DB25/DB56}* at 25°C), control (*nSyb-GAL4* at 25°C), *canA1* RNAi (JF) knockdown (*nSyb-GAL4/UAS-canA1-RNAi* (TRiP.JF01871) at 29°C), *canA1* RNAi (JF) knockdown plus Fwe overexpression (*nSyb-GAL4/UAS-canA1-RNAi* (TRiP.JF01871)/*UAS-HA-Fwe-APEX2* at 29°C). TEM processing was performed after the following treatments: at rest (10 min incubation of 5 mM K⁺/0 mM Ca²⁺); high K⁺ stimulation (10 min stimulation of 90 mM K⁺/2 mM Ca²⁺); 10 min recovery (10 min stimulation of 90 mM K⁺/2 mM Ca²⁺, followed by 10 min incubation of 5 mM K⁺/0 mM Ca²⁺); or 20 min recovery (10 min stimulation of 90 mM K⁺/2 mM Ca²⁺, followed by 20 min incubation of 5 mM K⁺/0 mM Ca²⁺). Bulk endosomes (>80 nm in diameter, red asterisks). Mitochondria (mt). (b) Quantification data of total numbers of bulk endosomes per bouton area. Individual data values are shown in graphs. p values: ns, not significant; *p<0.05; **p<0.01; ***p<0.001; ****p<0.0001. Mean ± SEM. Scale bar: 500 nm. Statistics: one-way ANOVA with Tukey's post hoc test.

The online version of this article includes the following source data and figure supplement(s) for figure 5:

Source data 1. Source data for **Figure 5**.

Figure supplement 1. Blockade of the positive feedback loop between Fwe and PI(4,5)P₂ abolishes SV reformation from the bulk endosome.

Figure supplement 1—source data 1. Source data for **Figure 5—figure supplement 1**.

reduced (**Figure 6d–f**), whereas there was only a mild reduction in its SV localization (**Figure 6d–e**). Therefore, in addition to initiating ADBE, PI(4,5)P₂ microdomains play a role in facilitating the retrieval of Fwe to the bulk endosome, enabling ADBE to remove its trigger via a negative feedback regulatory mechanism and reducing endocytosis to prevent excess membrane uptake.

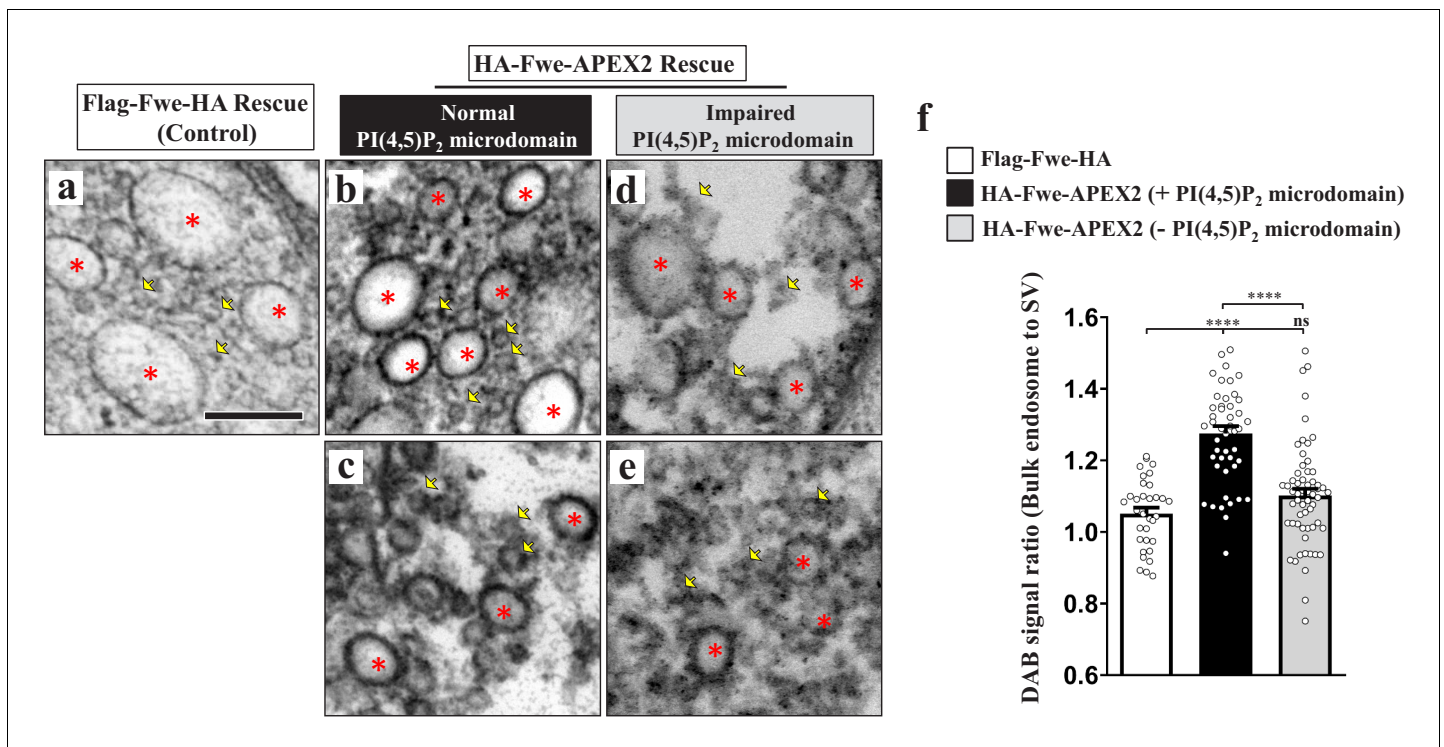


Figure 6. PI(4,5)P₂ facilitates recycling of Fwe to bulk endosomes. (a–f) PI(4,5)P₂ retrieves Fwe to bulk endosomes. (a–e) TEM images of the boutons of Flag-Fwe-HA rescue (*nSyb-GAL4/UAS-Flag-Fwe-HA* in *fwe^{DB25/DB56}* at 25°C, a), HA-Fwe-APEX2 rescue (*nSyb-GAL4/UAS-HA-Fwe-APEX2* in *fwe^{DB25/DB56}* at 25°C, b–c), or HA-Fwe-APEX2 rescue coexpressing Synj (*nSyb-GAL4/UAS-HA-Fwe-APEX2/UAS-synj* in *fwe^{DB25/DB56}* at 25°C, d–e). After high K⁺ stimulation, the boutons were subjected to DAB labeling. (a) The Flag-Fwe-HA rescue boutons presented DAB-negative bulk endosomes (red asterisks) and SVs (yellow arrows). (b and c) In the HA-Fwe-APEX2 rescue boutons, DAB signals on bulk endosomes (red asterisks) were higher than those on the SVs (yellow arrows). The views in b and c are from different boutons. (d and e) Under the condition of Synj overexpression, perturbation of PI(4,5)P₂ microdomain formation predominantly reduced DAB levels on the bulk endosomes (red asterisks). Views in d and e are from different boutons. (f) Quantification data for the DAB staining intensity ratio of bulk endosomes to surrounding SVs. The number of bulk endosomes, NMJ boutons, and larvae counted (Flag-Fwe-HA rescue control): Bulk endosomes (n = 33) derived from 5 NMJ boutons of two different larvae; HA-Fwe-APEX2 rescue: Bulk endosomes (n = 47) derived from 6 NMJ boutons of two different larvae; HA-Fwe-APEX2 rescue expressing Synj: Bulk endosomes (n = 59) derived from 9 NMJ boutons of two different larvae. Individual values were shown in graphs. p values: ns, not significant; ****p < 0.0001. Mean ± SEM. Scale bar: 200 nm (a–e). Statistics: one-way ANOVA with Tukey’s post hoc test.

The online version of this article includes the following source data and figure supplement(s) for figure 6:

Source data 1. Source data for **Figure 6**.

Figure supplement 1. HA-Fwe-APEX2 behaves like endogenous Fwe.

Discussion

ADBE occurs immediately after exocytosis to retrieve required SV protein and lipid constituents to further regenerate SVs under conditions of high-frequency stimulations. Here, we show that the Fwe Ca²⁺ channel-dependent compartmentalization of PI(4,5)P₂ orchestrates coupling of exocytosis to ADBE and subsequent SV reformation. Based on our findings, we propose a model for this interplay (depicted in **Figure 7**). Under conditions of strong stimulation, SV exocytosis transfers Fwe from SVs to the periaxial zone, where some of the activated Fwe provides the low Ca²⁺ levels that initiate Calcineurin activation to upregulate PI(4,5)P₂ (Step 1). Increased PI(4,5)P₂ enhances Fwe Ca²⁺ channel activity, thereby establishing a positive feedback loop that induces PI(4,5)P₂ microdomain formation (Step 2). High levels of PI(4,5)P₂ within these microdomains elicit bulk membrane invagination by triggering actin polymerization (Step 3). In parallel, PI(4,5)P₂ facilitates proper retrieval of Fwe to the bulk endosome (Step 4), thereby terminating the ADBE process. Finally, PI(4,5)P₂ microdomains dictate SV reformation from the bulk endosomes (Step 5), coordinating ADBE and subsequent SV reformation.

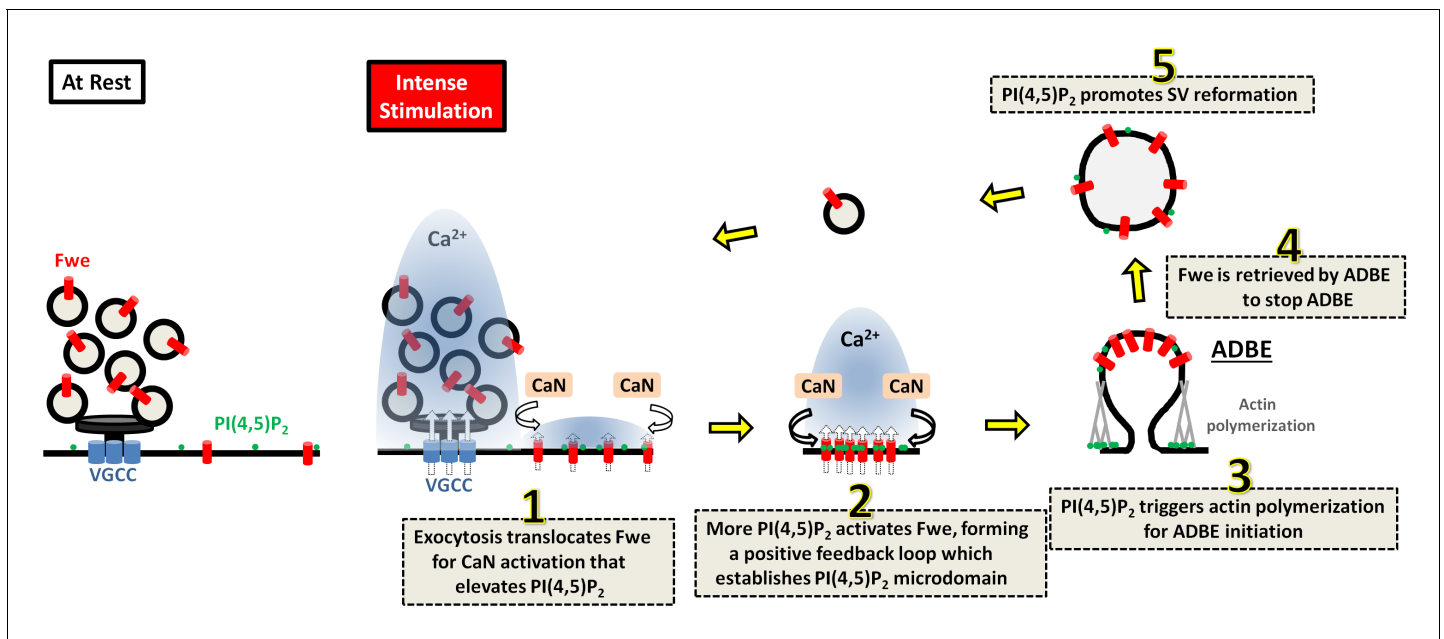


Figure 7. A proposed model for the role of Fwe-dependent PI(4,5)P₂ microdomains in coordinating ADBE and SV reformation from bulk endosomes. Details are described in the Discussion section.

Fwe-dependent PI(4,5)P₂ microdomains trigger ADBE

The role of actin polymerization in ADBE has been investigated in mammals (Kononenko *et al.*, 2014; Soykan *et al.*, 2017; Wu *et al.*, 2016), as well as in *Drosophila* (Akbergenova and Bykhovskaia, 2009). PI(4,5)P₂ is known to control a range of actin regulators, thereby modulating the dynamics of actin polymerization and branching (Janmey *et al.*, 2018). It has been shown previously that, in response to nicotine stimulation, PI(4,5)P₂ forms clustered microdomains of sub-micrometer scale prior to the appearance of an actin-based ring structure in bovine chromaffin cells (Gormal *et al.*, 2015). In agreement with this observation, we show that intense activity stimulation drives the formation of PI(4,5)P₂ microdomains at the periaxial zone of *Drosophila* NMJ synaptic boutons. Perturbations of the formation of these microdomains reduces ADBE activity very significantly, demonstrating that rapid accumulation of PI(4,5)P₂ in microdomains is needed to trigger extensive actin polymerization, which likely generates sufficient mechanical force to produce the large endosomes. Furthermore, loss of *fwe* or RNAi-mediated calcineurin knockdown effectively inhibited PI(4,5)P₂ microdomain formation and, as a consequence, ADBE. Those results are consistent with previous data supporting that Ca²⁺ promotes ADBE by activating its sensor Calcineurin (Cousin and Robinson, 2001; Jin *et al.*, 2019; Sun *et al.*, 2010; Wu *et al.*, 2009; Wu *et al.*, 2014b; Xue *et al.*, 2011).

Our data provide evidence that Fwe-derived Ca²⁺ regulates PI(4,5)P₂ dynamics through activation of Calcineurin. Phosphatidylinositol 4-phosphate 5-kinases (PIP5Ks) are the major kinases that promote PI(4,5)P₂ production from precursor phosphoinositides (van den Bout and Divecha, 2009). At mammalian central synapses, PIP5Kγ661, one of the PIP5Kγ isoforms, is the most abundant relative to other isoforms (Wenk *et al.*, 2001). Activation of PIP5Ks can be engaged by binding to its regulators (van den Bout and Divecha, 2009). In response to Ca²⁺ activation, Calcineurin has been shown to dephosphorylate PIP5Kγ661 to promote its interaction with AP-2 complexes, which augments the enzymatic activity of PIP5Kγ661 (Nakano-Kobayashi *et al.*, 2007). Synj is the major PI(4,5)P₂ phosphatase in neurons (Tsujiyama *et al.*, 2001) and it is involved in the SV endocytosis prompted by strong stimulation (Mani *et al.*, 2007). Whereas phosphorylation of Synj by CDK5 inhibits its activity, Calcineurin enhances Synj activity via dephosphorylation (Lee *et al.*, 2004). In yeasts, cells undergo bulk membrane invagination, a process reminiscent of neuronal ADBE, under conditions of hyperosmotic stress (Guiney *et al.*, 2015). However, in that process, Calcineurin dephosphorylates Synj to

alter its association with other endocytic partners rather than affecting its enzymatic activity to regulate PI(4,5)P₂ distribution. Intriguingly, divalent Ca²⁺ ions are known to control the lateral organization of PI(4,5)P₂, further compartmentalizing PI(4,5)P₂ into ~70 nm-sized microdomains in monolayers of lipid bilayers via electrostatic interactions between Ca²⁺ and PI(4,5)P₂ (Carvalho et al., 2008; Ellenbroek et al., 2011; Levental et al., 2009; Sarmiento et al., 2014; Wang et al., 2012; Wen et al., 2018). Similarly-sized PI(4,5)P₂ clusters have been observed in PC12 cells under non-stimulated conditions (van den Bogaart et al., 2011). Therefore, tight spatial and temporal control of the localizations and activities of Fwe, Calcineurin, PIP5K, and Synj may drive Ca²⁺-mediated PI(4,5)P₂ clustering, perhaps accounting for the Fwe-dependent formation of PI(4,5)P₂ microdomains at the periactive zone prior to ADBE. Further investigations are needed to characterize the underlying mechanisms.

Our data show that direct binding of PI(4,5)P₂ is required for the Ca²⁺ channel activity of Fwe. Perturbation of PI(4,5)P₂-Fwe binding further impaired the formation of PI(4,5)P₂ microdomains as well as ADBE initiation. Hence, PI(4,5)P₂ controls Fwe gating, so that Fwe can promote PI(4,5)P₂ compartmentalization through positive feedback regulation. Furthermore, loss of Fwe impaired the intracellular Ca²⁺ increase that was evoked upon strong activity stimulation (Figure 3g; Yao et al., 2017). These results support that, in addition to PI(4,5)P₂, the channel function of Fwe may be gated by a significant change in membrane potential. Expanding on that notion, it is therefore possible that both factors may gate Fwe, thereby only allowing channel opening when exocytosis directs Fwe to periactive zones. Future studies should explore the details of this channel gating mechanism.

PI(4,5)P₂ microdomains coordinate retrieval of SV membranes and proteins for SV reformation via ADBE

Since ADBE is triggered very rapidly by intense stimuli, it was thought that this type of recycling randomly retrieves SV proteins and that the sorting process takes place when SVs regenerate from bulk endosomes. However, recent work has highlighted a distinct retrieval route for SV proteins during ADBE (Kokotos et al., 2018; Nicholson-Fish et al., 2015). Very little is known about the mechanisms underlying that retrieval route. Interestingly, removing VAMP4 or mutating its di-leucine motif was shown to impair ADBE (Nicholson-Fish et al., 2015). The di-leucine motif of transmembrane proteins is known to mediate binding with the AP-2 adaptor complex (Traub and Bonifacino, 2013). Given that the AP-2 adaptor complex works closely with PI(4,5)P₂ (McMahon and Boucrot, 2011), these findings imply a role for PI(4,5)P₂ and the AP-2 adaptor complex in SV protein sorting via ADBE. Indeed, our data show that bulk endosomes recycle few in a PI(4,5)P₂ microdomain-dependent manner. Hence, in addition to initiating ADBE, PI(4,5)P₂ may participate in SV protein sorting to bulk endosomes.

SV regeneration occurs following formation of the bulk endosome. Our results also show that either removing Fwe-derived Ca²⁺ or perturbing PI(4,5)P₂ activity impaired the ability of SVs to reform from the bulk endosome, highlighting the essential role of PI(4,5)P₂ microdomains in this process. How could PI(4,5)P₂ of the plasma membrane regulate subsequent SV reformation? It has been shown that PI(4,5)P₂ is rapidly downregulated on bulk endosomes once formed by ADBE (Chang-Ileto et al., 2011; Cremona et al., 1999; Milosevic et al., 2011). It is conceivable that the high concentrations of PI(4,5)P₂ in microdomains may compensate for rapid turnover, thereby ensuring appropriate concentrations of PI(4,5)P₂ or PI(4)P for further recruitment of clathrin and adaptor protein complexes, such as AP-1 and AP-2 (Blumstein et al., 2001; Cheung and Cousin, 2012; Faúndez et al., 1998; Glyvuk et al., 2010; Kokotos et al., 2018; Kononenko et al., 2014; Park et al., 2016). Alternatively, PI(4,5)P₂ may facilitate SV protein sorting prior to ADBE, meaning proper SV protein compositions on bulk endosomes could control recruitment of adaptor protein complexes. Both of these potential mechanisms are not mutually exclusive and may operate in parallel. Therefore, we propose that the Fwe-dependent formation of PI(4,5)P₂ microdomains is potentially important in coordinating retrieval of SV membranes and cargos when SVs are recycled via ADBE. Notably, the Fwe channel is evolutionarily conserved from yeast to human (Yao et al., 2009). We have also previously demonstrated conserved functions of Fwe in CME and ADBE at the mammalian central synapse (Yao et al., 2017). A recent study has also identified Fwe as a key protein mediating Ca²⁺-dependent granule endocytosis in mouse cytotoxic T lymphocytes (Chang et al., 2018). Hence, we hypothesize that the mechanism of ADBE we report here may be generally deployed across synapses and species, even in other non-neuronal cells.

Materials and methods

Drosophila strains and genetics

five mutants and transgenes: *fwe*^{DB25} and *fwe*^{DB56} (Yao et al., 2009); UAS-Flag-Fwe-HA (Yao et al., 2009); UAS-Flag-Fwe[E79Q]-HA (Yao et al., 2017); UAS-*canA1*-RNAi(FB4) (Dijkers and O'Farrell, 2007); UAS-*canA1*-RNAi(TRiP.JF01871) (Bloomington Drosophila Stock Center, BDSC#25850); UAS-*synj* (Khuong et al., 2013); UAS-PLC_{δ1}-PH-EGFP (Verstreken et al., 2009) (Bloomington Drosophila Stock Center, BDSC#39693); UAS-PLC_{δ1}-PHS39R-EGFP (Verstreken et al., 2009) (Bloomington Drosophila Stock Center, BDSC#39694); *nSyb*-GAL4 (Pauli et al., 2008); UAS-*mCD8*-EGFP (Kyoto Stock Center, DGRC#108068); *vglut*-*lexA* (Bloomington Drosophila Stock Center, BDSC #60314); 13XLex-*Aop2*-IVS-GCaMP6f (Bloomington Drosophila Stock Center, BDSC #44277); *synj*¹ (Verstreken et al., 2003) (Bloomington Drosophila Stock Center, BDSC#24883); LexAop2-PLC_{δ1}-PH-APEX2-HA (This paper); and LexAop2-PLC_{δ1}-PH-EGFP (This paper). Fly stocks were reared on regular food at 25°C or as otherwise indicated.

Molecular cloning and transgenesis

For pUAST-HA-Fwe[WT]-APEX2, the coding sequence of the Fwe B isoform and APEX2 were separately PCR-amplified from pUAST-Flag-Fwe-HA (Yao et al., 2009) or pcDNA3 APEX2-NES (addgene #49386), respectively, and then subcloned into the pUAST vector. pUAST-HA-Fwe[K29A/R33A]-APEX2-HA was generated from pUAST-HA-Fwe[WT]-APEX2 through site-directed mutagenesis. pUAST-Flag-Fwe [K29/R33/K95/K100/R105/K146A/K147A/R150A]-HA, pUAST-Flag-Fwe[K146A/K147A/R150A]-HA and pUAST-Flag-Fwe[K95/K100/R105A]-HA were generated from pUAST-Flag-Fwe-HA through site-directed mutagenesis. For plexAop2-PLC_{δ1}-PH-APEX2-HA, the coding sequence of the PLC_{δ1}-PH domain and APEX2-HA were separately PCR-amplified and then subcloned into pJFRC19-13XLexAop2-IVS-myr:GFP (addgene #26224). For plexAop2-PLC_{δ1}-PH-EGFP, the coding sequence of PLC_{δ1}-PH-EGFP was PCR-amplified from genomic DNA of the UAS-PLC_{δ1}-PHS39R-EGFP fly stock and then subcloned into pJFRC19-13XLexAop2-IVS-myr:GFP. For YeMP-Nluc-Fwe-1D4, the cDNA fragment of Nluc and Fwe-1D4 was PCR-amplified from pNL1.1[Nluc] (a gift from Yi-Shiuan Huang) and YeMP-Fwe-1D4 plasmid (Yao et al., 2009), respectively, and then subcloned into the yeast expression YeMP vector. For YeMP-Nluc-Fwe[K29A/R33A]-1D4, YeMP-Nluc-Fwe[K95/K100/R105/K146/K147/R150A]-1D4, and YeMP-Nluc-Fwe[K29/R33/K95/K100/R105/K146/K147/R150A]-1D4, the DNA fragments of the Fwe variant were PCR-amplified from pUAST plasmids and subcloned into the YeMP-Nluc-Fwe-1D4 vector. PCR primers are indicated in key source table (Appendix 1). Transgenic flies were made by WellGenetics Inc.

Immunohistochemistry

Third instar larvae were fixed with 4% paraformaldehyde for 20 min. We used 1xPBS buffer containing 0.1% Tween-20 to stain the HA-tagged Fwe proteins. We used 1xPBS buffer containing 0.1% Triton X 100 to stain PLC_{δ1}-PH-EGFP or AP-2α. We used 1xPBS buffer containing 0.2% Triton X 100 to stain GCaMP6f. Primary antibodies were used as follows: guinea pig α-Fwe B isoform (1:400) (Yao et al., 2017), chicken α-GFP (Invitrogen, 1:500); mouse α-HA (Sigma, 1:400), mouse α-Bruchpilot (Developmental Studies Hybridoma Bank nc82, 1:100); rabbit α-AP-2α (1:3000) (González-Gaitán and Jäckle, 1997) guinea pig α-Eps15 (1:3000) (Koh et al., 2007); rabbit α-HRP conjugated with Alexa Fluor 488, Cy3 or Cy5 (Jackson ImmunoResearch Laboratories, 1:250). Secondary antibodies conjugated to Alexa Fluor 488, Alexa Fluor 555, or Alexa Fluor 647 (Invitrogen and Jackson ImmunoResearch) were used at 1:500. The NMJ boutons were derived from muscles 6 and 7 of abdominal segments 2/3. To detect PI(4,5)P₂ microdomains, the NMJ boutons were fixed immediately after high K⁺ stimulation. To quantitatively compare PLC_{δ1}-PH-EGFP or AP-2α immunostaining signal among different sets of experiments, fixed larval fillets derived from different conditions were collected into the same Eppendorf tube. The NMJ boutons were stained for PLC_{δ1}-PH-EGFP using α-GFP and for the neuronal membranes using fluorescein-conjugated α-HRP. Consecutive single-plane images of the boutons of muscles 6 and 7 in abdominal segments 2 or 3 of all different experimental sets were taken using a Zeiss LSM 780 confocal microscope with a Plan-Apochromat 63x/1.4 Oil DIC M27 objective under a 1 μm interval setup and equal laser power and laser exposure time. For data quantification, single-plane images of five different individual boutons from each NMJ

bouton image were used. The presynaptic plasma membrane regions of the type Ib boutons defined by α -HRP immunostaining were outlined manually, and native fluorescence or α -GFP immunostaining signal intensities of PLC $_{\delta 1}$ -PH-EGFP or AP-2 α on the plasma membrane were quantified using ImageJ and averaged to serve as one individual data-point. For data quantification of SIM images, we chose single-plane SIM images focused on a central section of an individual bouton and outlined plasma membrane-associated PLC $_{\delta 1}$ -PH-EGFP-immunostained clusters using ImageJ. The area of these clusters of each individual bouton was measured using ImageJ, and the areas of clusters measuring over 0.032 μm^2 (equal to a \sim 200 nm diameter circle, i.e. the resolution limit of SIM) were averaged to serve as one data-point. We assessed 37 boutons derived from five NMJs of three different larvae. Image processing was achieved using LSM Zen.

Western blot

For western blotting, the brain and ventral nerve chord of larval fillets were removed and subjected to different stimulation conditions. Afterwards, the fillets were crushed in 1xSDS sample buffer and boiled for 5 min. Dilutions for primary antibodies were as follows: mouse anti- α -actin, 1:20000 (Sigma); chicken anti-GFP, 1:5000 (Invitrogen).

PLA

Third-instar larvae were fixed with 4% paraformaldehyde for 20 min and permeabilized with 1xPBS buffer containing 0.1% Tween-20. Larval fillets were incubated with mouse α -HA (Sigma, 1:200) and rabbit α -GFP (Invitrogen, 1:500) in 1xPBS buffer containing 0.1% Tween-20 at 4°C for 12 hr. Excess antibodies were washed out using 1xPBS buffer containing 0.1% Tween-20. The samples were mixed with the PLA probe (Sigma, 1:5) for 2 hr at 37°C. After washing with 1x buffer A, the samples were incubated with ligation solution (1:40) for 1.5 hr at 37°C. After again washing with 1x buffer A, the samples were incubated with amplification solution (1:80) for 2 hr at 37°C. Next, the samples were washed with 1x buffer B and then 0.01x buffer B. The samples were stained with anti-chicken Alexa Fluor 488-conjugated IgG and anti-mouse Alexa Fluor 647-conjugated IgG, followed by a wash of 1x PBS buffer containing 0.1% Tween-20. To quantitatively compare PLA signal, fixed larval fillets derived from different experimental conditions were collected into the same Eppendorf tube and processed. Consecutive single-plane images of the boutons of muscles 6 and 7 in abdominal segments 2 or 3 of all different experimental sets were taken using a Zeiss LSM 780 confocal microscope with a Plan-Apochromat 63x/1.4 Oil DIC M27 objective under a 1 μm interval setup and equal laser power and laser exposure time. For data quantification, consecutive Z-plane images spanning whole NMJ were projected under maximal fluorescence intensity. All type Ib boutons in individual Z-projection image were outlined according to PLC $_{\delta 1}$ -PH-EGFP-stained regions. PLA or antibody immunostaining signal intensities within the boutons and background staining signals in surrounding muscles were counted using ImageJ and averaged. One individual data-point was obtained by muscular background signal subtraction. Image processing was achieved using LSM Zen.

Nluc-Fwe-1D4 purification and BRET assay

The Nluc-Fwe-1D4 fusion protein was purified as described previously (Yao *et al.*, 2009). Briefly, plasma membrane was isolated from a two liter culture of yeast strain BJ5457 expressing Nluc-Fwe-1D4 protein. The plasma membranes were solubilized at 4°C with 10x critical micelle concentration (CMC) DDM (Anatrace) in a solution of 20 mM HEPES (pH8.0), 300 mM NaCl, 10% Glycerol, 2.0 mM DTT, and 1 mM PMSF for 2 hr. Insoluble membranes were spun down by centrifugation at 100,000 $\times g$ for 60 min. The lysates including solubilized Nluc-Fwe-1D4 proteins were cleaned with CNBr sepharose 4B at 4°C for 1 hr. The samples were then mixed with α -1D4-conjugated CNBr-activated Sepharose 4B at 4°C for 8–12 hr. After washing with a solution of 20 mM HEPES (pH8.0), 150 mM NaCl, 10% Glycerol, 2.0 mM DTT, 1 mM PMSF and 2.6xCMC DDM, the protein was eluted with a 1D4 peptide-containing buffer (3 mg of 1D4 peptide in 1 ml of washing buffer). Purified proteins were subjected to SDS-PAGE and detected using Lumitein staining or western blotting with anti- α -1D4 antibody at 1:5000 (Yao *et al.*, 2009). The BRET assay was performed in a 384-well plate, with each well containing 30 μl of reaction solution [0.5 nM purified proteins, 5 μM BODIPY-TMR Phosphatidylinositol 4,5-bisphosphate (C-45M16A, Echelon Bioscience), furimazine (Promega, 1:2000), 20 mM HEPES, 150 mM NaCl, 10% Glycerol, 2 mM DTT, 1mM PMSF, 4 mM DDM].

Fluorescence signal was detected using a Microplate Reader M1000 pro (Tecan) with two different emission spectrum filters, that is 500–540 nm for Nluc and 550–630 nm for BODIPY-TMR Phosphatidylinositol 4,5-bisphosphate. For competition assay, 30 μ l of the reaction solution was included with 1 mM brain phosphatidylinositol 4,5-bisphosphate (Avanti). The BRET signal was calculated according to the following formula:

Live imaging

For PLC $_{\delta 1}$ -PH-EGFP imaging, third-instar larvae were dissected in a zero-calcium HL-3 solution at room temperature. For groups stimulated with electric pulses, larval fillets were bathed in a solution of 2 mM Ca $^{2+}$ (70 mM NaCl, 5 mM KCl, 10 mM MgCl $_2$, 10 mM NaHCO $_3$, 5 mM trehalose, 5 mM HEPES (pH 7.4), 115 mM sucrose, 2 mM CaCl $_2$). High concentrations of glutamate were used to desensitize glutamate receptors, thereby reducing muscle contraction when stimulated. A cut axonal bundle was sucked into the tip of a glass capillary electrode and then stimulated at 20 or 40 Hz for 3 min. Stimulus strength was set at 5 V and 0.5 ms duration by means of pClamp 10.6 software (Axon Instruments Inc). Ten images were taken from larval fillets at rest. After stimulation for 2 min, muscle contraction significantly decelerated. Thus, we captured 60 consecutive snapshot images every second from the third minute. Muscles 6 and 7 of abdominal segment three were imaged. Under the condition of high K $^{+}$ stimulation, larval fillets were bathed in a solution of 90 mM K $^{+}$ /2 mM Ca $^{2+}$ /7 mM glutamate (25 mM NaCl, 90 mM KCl, 10 mM MgCl $_2$, 10 mM NaHCO $_3$, 5 mM trehalose, 5 mM HEPES (pH 7.4), 30 mM sucrose, 2 mM CaCl $_2$, 7 mM monosodium glutamate) for 5 min. Sixty consecutive snapshot images were captured every second from the fifth minute of stimulation. Images were taken using a long working distance water immersion objective (XLUMPLFLN20XW, Olympus) and EMCCD camera (iXon, Andor) mounted on a SliceScope Pro 6000 (Scientifica) microscope and employing MetaFluor software (Molecular Devices). For GCaMP6f imaging, third instar larvae were dissected in a zero-calcium HL-3 solution at room temperature. Ten images were taken from larval fillets at rest. Subsequently, larval fillets were stimulated with a solution of 90 mM K $^{+}$ /2 mM Ca $^{2+}$ /7 mM glutamate for 5 min. Sixty consecutive snapshot images were captured every second from the fifth minute of stimulation. The *lexA/lexAop2* binary system was used to stably express a comparable level of GCaMP6f in the presynaptic compartment of NMJ boutons for all tested genotypes, allowing us to compare Ca $^{2+}$ imaging results when the resting Ca $^{2+}$ levels were potentially affected by differences in genetic background. We stained for the GCaMP6f protein using a-GFP antibody and confirmed comparable GCaMP6f levels among the different genotypes tested in each dataset. Evoked Ca $^{2+}$ levels were calculated by subtracting the resting GCaMP6f fluorescence from the GCaMP6f fluorescence induced by high K $^{+}$ stimulation. The NMJs were derived from muscles 6 and 7 of abdominal segment 2/3. Images were taken using a water immersion objective (W Plan-Apochromat 40x/1.0 DIC M27, Zeiss). For each imaging experiment, at least three focused images for the same boutons under resting, stimulation, or post-stimulation conditions were used for data quantification. Fluorescence intensities of PLC $_{\delta 1}$ -PH-EGFP or GCaMP6f within the boutons were quantified using ImageJ and averaged to serve as one individual data-point. Image processing was achieved using LSM Zen.

Transmission electron microscopy

Third instar larval fillets were prepared in zero-calcium HL-3 solution at room temperature. For the resting conditions, the fillets were bathed in zero-calcium HL-3 solution at room temperature for another 10 min before fixation. For the high K $^{+}$ stimulation conditions, fillets were bathed in a solution of 90 mM K $^{+}$ and 2 mM Ca $^{2+}$ for 10 min. The stimulation was terminated by washing three times with zero-calcium HL-3 solution, followed by fixation. For recovery conditions, following high K $^{+}$ stimulation, fillets were bathed in zero-calcium HL-3 solution at room temperature for 10 or 20 min before fixation. Larval fillets were fixed for 12 hr at 4°C in 4% paraformaldehyde/1% glutaraldehyde/0.1 M cacodylic acid (pH 7.2), rinsed with 0.1 M cacodylic acid (pH 7.2), and postfixed with 1% OsO $_4$ and 0.1 M cacodylic acid at room temperature for 3 hr. These samples were then subjected to a series of dehydration steps using 30–100% ethanol. After 100% ethanol dehydration, the samples were sequentially incubated with propylene, a mixture of propylene and resin, and pure resin. Finally, the samples were embedded in 100% resin. TEM images were captured using Tecnai G2 Spirit TWIN (FEI Company) and a Gatan CCD Camera (794.10.BP2MultiScanTM). NMJ boutons were

captured at high magnifications. For each condition, NMJ bouton images were taken from at least five different NMJs of each third-instar larvae, and three to five larvae were used. Quantifications were performed using ImageJ. For diaminobenzidine (DAB) polymerization, third instar larvae were dissected at room temperature in zero-calcium HL-3 medium, followed by a 10 min incubation in 5 mM K^+ /0 Ca^{2+} mM solution or a 10 min stimulation of 90 mM K^+ /2 mM Ca^{2+} . Next, the samples were subjected to 30 min fixation in ice-cold 4% paraformaldehyde/1% glutaraldehyde/0.1 M cacodylic acid (pH 7.2). Subsequently, the samples were transferred to Eppendorf tubes for 15 min incubation with a solution of 0.5 mg/ml DAB solution, followed by incubation with a solution of 0.5 mg/ml DAB and 0.006% H_2O_2 for 15 min at room temperature. This latter step was repeated once to ensure DAB polymerization. Samples were washed three times with 1xPBS buffer for 10 min and then fixed with a solution of 4% paraformaldehyde/1% glutaraldehyde/0.1 M cacodylic acid (pH 7.2) for 12 hr at 4°C, followed by fixation with a solution of 1% OsO_4 /0.1 M cacodylic acid at room temperature for 3 hr. Then, standard dehydration, embedding, and imaging were performed. For data quantifications of DAB intensities, the display color of TEM images was reverted to grayscale using ImageJ. Average DAB staining intensity on each individual bulk endosome was quantified. Then, the average DAB staining intensity on 50–100 surrounding SVs from the same bouton image was used to assess the relative level of HA-Fwe-APEX2 on bulk endosomes vs SVs.

Statistics

All data analyses were conducted using GraphPad Prism 8.0, unless stated otherwise. Paired and multiple datasets were compared by Student t-test or one-way ANOVA with Tukey's post hoc test, respectively. Individual data values are biological replicates. Samples were randomized during preparation, imaging, and data processing to minimize bias.

Acknowledgements

We thank Hugo Bellen, Patrik Verstreken, Kartik Venkatachalam, the Bloomington *Drosophila* Stock Center, and the Developmental Studies Hybridoma Bank for stocks and reagents. We thank Hugo Bellen, Ruey-Hwa Chen, and Y Henry Sun for the critical comments. We thank Yi-Shui Huang for providing the Nluc plasmid. We thank DNA Sequencing Core Facility (AS-CFII-108–115) for sequencing DNA constructs. We thank Wellgenetics for making transgenic lines. We thank the IMB imaging core for helping with TEM and SIM imaging. This work was supported by grants from the Ministry of Science and Technology of Taiwan (107–2311-B-001–003-MY3, 106-0210-01-15-02, and 107-0210-01-19-01).

Additional information

Funding

Funder	Grant reference number	Author
Ministry of Science and Technology, Taiwan	107-2311-B-001-003-MY3	Chi-Kuang Yao
Ministry of Science and Technology, Taiwan	106-0210-01-15-02	Chi-Kuang Yao
Ministry of Science and Technology, Taiwan	107-0210-01-19-01	Chi-Kuang Yao

The funders had no role in study design, data collection and interpretation, or the decision to submit the work for publication.

Author contributions

Tsai-Ning Li, Yu-Jung Chen, Conceptualization, Resources, Data curation, Software, Formal analysis, Validation, Investigation, Visualization, Methodology, Project administration, Writing - review and editing; Ting-Yi Lu, Data curation, Formal analysis, Investigation, Methodology; You-Tung Wang, Hsin-Chieh Lin, Resources, Data curation, Software, Formal analysis, Validation, Investigation, Visualization, Methodology; Chi-Kuang Yao, Conceptualization, Resources, Data curation, Software, Formal

analysis, Supervision, Funding acquisition, Validation, Investigation, Visualization, Methodology, Writing - original draft, Project administration, Writing - review and editing

Author ORCIDs

Tsai-Ning Li  <https://orcid.org/0000-0003-0195-145X>

Chi-Kuang Yao  <https://orcid.org/0000-0003-0977-4347>

Decision letter and Author response

Decision letter <https://doi.org/10.7554/eLife.60125.sa1>

Author response <https://doi.org/10.7554/eLife.60125.sa2>

Additional files

Supplementary files

- Transparent reporting form

Data availability

All data generated or analysed during this study are included in the manuscript and supporting files. Source data files have been provided.

References

- Akbergenova Y**, Bykhovskaia M. 2009. Enhancement of the endosomal endocytic pathway increases quantal size. *Molecular and Cellular Neuroscience* **40**:199–206. DOI: <https://doi.org/10.1016/j.mcn.2008.10.005>, PMID: 19026748
- Aoyagi K**, Sugaya T, Umeda M, Yamamoto S, Terakawa S, Takahashi M. 2005. The activation of exocytotic sites by the formation of phosphatidylinositol 4,5-Bisphosphate microdomains at syntaxin clusters. *Journal of Biological Chemistry* **280**:17346–17352. DOI: <https://doi.org/10.1074/jbc.M413307200>
- Blumstein J**, Faundez V, Nakatsu F, Saito T, Ohno H, Kelly RB. 2001. The neuronal form of adaptor protein-3 is required for synaptic vesicle formation from endosomes. *The Journal of Neuroscience* **21**:8034–8042. DOI: <https://doi.org/10.1523/JNEUROSCI.21-20-08034.2001>, PMID: 11588176
- Brand AH**, Perrimon N. 1993. Targeted gene expression as a means of altering cell fates and generating dominant phenotypes. *Development* **118**:401–415. PMID: 8223268
- Cabanos C**, Wang M, Han X, Hansen SB. 2017. A soluble fluorescent binding assay reveals PIP₂ Antagonism of TREK-1 Channels. *Cell Reports* **20**:1287–1294. DOI: <https://doi.org/10.1016/j.celrep.2017.07.034>, PMID: 28793254
- Carvalho K**, Ramos L, Roy C, Picart C. 2008. Giant unilamellar vesicles containing phosphatidylinositol(4,5) bisphosphate: characterization and functionality. *Biophysical Journal* **95**:4348–4360. DOI: <https://doi.org/10.1529/biophysj.107.126912>, PMID: 18502807
- Chanaday NL**, Cousin MA, Milosevic I, Watanabe S, Morgan JR. 2019. The synaptic vesicle cycle revisited: new insights into the modes and mechanisms. *The Journal of Neuroscience* **39**:8209–8216. DOI: <https://doi.org/10.1523/JNEUROSCI.1158-19.2019>, PMID: 31619489
- Chang H-F**, Mannebach S, Beck A, Ravichandran K, Krause E, Frohnweiler K, Fecher-Trost C, Schirra C, Pattu V, Flockerzi V, Rettig J. 2018. Cytotoxic granule endocytosis depends on the flower protein. *Journal of Cell Biology* **217**:667–683. DOI: <https://doi.org/10.1083/jcb.201706053>
- Chang-Ileto B**, Frere SG, Chan RB, Voronov SV, Roux A, Di Paolo G. 2011. Synaptojanin 1-mediated PI(4,5)P₂ hydrolysis is modulated by membrane curvature and facilitates membrane fission. *Developmental Cell* **20**:206–218. DOI: <https://doi.org/10.1016/j.devcel.2010.12.008>, PMID: 21316588
- Chen TW**, Wardill TJ, Sun Y, Pulver SR, Renninger SL, Baohan A, Schreiter ER, Kerr RA, Orger MB, Jayaraman V, Looger LL, Svoboda K, Kim DS. 2013. Ultrasensitive fluorescent proteins for imaging neuronal activity. *Nature* **499**:295–300. DOI: <https://doi.org/10.1038/nature12354>, PMID: 23868258
- Chen CK**, Bregere C, Paluch J, Lu JF, Dickman DK, Chang KT. 2014. Activity-dependent facilitation of synaptojanin and synaptic vesicle recycling by the minibrain kinase. *Nature Communications* **5**:4246. DOI: <https://doi.org/10.1038/ncomms5246>, PMID: 24977345
- Chen X**, Khajeh JA, Ju JH, Gupta YK, Stanley CB, Do C, Heller WT, Aggarwal AK, Callaway DJE, Bu Z. 2015. Phosphatidylinositol 4,5-Bisphosphate clusters the cell adhesion molecule CD44 and assembles a specific CD44-Ezrin heterocomplex, as revealed by small angle neutron scattering. *Journal of Biological Chemistry* **290**:6639–6652. DOI: <https://doi.org/10.1074/jbc.M114.589523>
- Cheung G**, Jupp OJ, Cousin MA. 2010. Activity-Dependent bulk endocytosis and Clathrin-Dependent endocytosis replenish specific synaptic vesicle pools in central nerve terminals. *Journal of Neuroscience* **30**:8151–8161. DOI: <https://doi.org/10.1523/JNEUROSCI.0293-10.2010>

- Cheung G**, Cousin MA. 2012. Adaptor protein complexes 1 and 3 are essential for generation of synaptic vesicles from activity-dependent bulk endosomes. *Journal of Neuroscience* **32**:6014–6023. DOI: <https://doi.org/10.1523/JNEUROSCI.6305-11.2012>, PMID: 22539861
- Clayton EL**, Evans GJ, Cousin MA. 2008. Bulk synaptic vesicle endocytosis is rapidly triggered during strong stimulation. *Journal of Neuroscience* **28**:6627–6632. DOI: <https://doi.org/10.1523/JNEUROSCI.1445-08.2008>, PMID: 18579735
- Cousin MA**, Robinson PJ. 2001. The dephosphins: dephosphorylation by calcineurin triggers synaptic vesicle endocytosis. *Trends in Neurosciences* **24**:659–665. DOI: [https://doi.org/10.1016/S0166-2236\(00\)01930-5](https://doi.org/10.1016/S0166-2236(00)01930-5), PMID: 11672811
- Cremona O**, Di Paolo G, Wenk MR, Lüthi A, Kim WT, Takei K, Daniell L, Nemoto Y, Shears SB, Flavell RA, McCormick DA, De Camilli P. 1999. Essential role of phosphoinositide metabolism in synaptic vesicle recycling. *Cell* **99**:179–188. DOI: [https://doi.org/10.1016/S0092-8674\(00\)81649-9](https://doi.org/10.1016/S0092-8674(00)81649-9), PMID: 10535736
- D’Avino PP**, Thummel CS. 1999. Ectopic expression systems in *Drosophila*. *Methods in Enzymology* **306**:129–142. DOI: [https://doi.org/10.1016/s0076-6879\(99\)06009-7](https://doi.org/10.1016/s0076-6879(99)06009-7), PMID: 10432451
- Dijkers PF**, O’Farrell PH. 2007. *Drosophila* calcineurin promotes induction of innate immune responses. *Current Biology* **17**:2087–2093. DOI: <https://doi.org/10.1016/j.cub.2007.11.001>, PMID: 18060786
- Ellenbroek WG**, Wang YH, Christian DA, Discher DE, Janmey PA, Liu AJ. 2011. Divalent cation-dependent formation of electrostatic PIP2 clusters in lipid monolayers. *Biophysical Journal* **101**:2178–2184. DOI: <https://doi.org/10.1016/j.bpj.2011.09.039>, PMID: 22067156
- Evans GJ**, Cousin MA. 2007. Activity-dependent control of slow synaptic vesicle endocytosis by cyclin-dependent kinase 5. *Journal of Neuroscience* **27**:401–411. DOI: <https://doi.org/10.1523/JNEUROSCI.3809-06.2007>, PMID: 17215401
- Faúndez V**, Horng JT, Kelly RB. 1998. A function for the AP3 coat complex in synaptic vesicle formation from endosomes. *Cell* **93**:423–432. DOI: [https://doi.org/10.1016/S0092-8674\(00\)81170-8](https://doi.org/10.1016/S0092-8674(00)81170-8), PMID: 9590176
- Gaffield MA**, Romberg CF, Betz WJ. 2011. Live imaging of bulk endocytosis in frog motor nerve terminals using FM dyes. *Journal of Neurophysiology* **106**:599–607. DOI: <https://doi.org/10.1152/jn.00123.2011>, PMID: 21543750
- Glyvuk N**, Tsytysyura Y, Geumann C, D’Hooge R, Hüve J, Kratzke M, Baltés J, Boening D, Böning D, Klingauf J, Schu P. 2010. AP-1/sigma1B-adaptin mediates endosomal synaptic vesicle recycling, learning and memory. *The EMBO Journal* **29**:1318–1330. DOI: <https://doi.org/10.1038/emboj.2010.15>, PMID: 20203623
- González-Gaitán M**, Jäckle H. 1997. Role of *Drosophila* alpha-adaptin in presynaptic vesicle recycling. *Cell* **88**:767–776. DOI: [https://doi.org/10.1016/S0092-8674\(00\)81923-6](https://doi.org/10.1016/S0092-8674(00)81923-6), PMID: 9118220
- Gormal RS**, Nguyen TH, Martin S, Papadopulos A, Meunier FA. 2015. An Acto-Myosin II constricting ring initiates the fission of Activity-Dependent bulk endosomes in neurosecretory cells. *Journal of Neuroscience* **35**:1380–1389. DOI: <https://doi.org/10.1523/JNEUROSCI.3228-14.2015>
- Granseth B**, Odermatt B, Royle SJ, Lagnado L. 2006. Clathrin-mediated endocytosis is the dominant mechanism of vesicle retrieval at hippocampal synapses. *Neuron* **51**:773–786. DOI: <https://doi.org/10.1016/j.neuron.2006.08.029>, PMID: 16982422
- Guiney EL**, Goldman AR, Elias JE, Cyert MS. 2015. Calcineurin regulates the yeast synaptojanin Inp53/Sjl3 during membrane stress. *Molecular Biology of the Cell* **26**:769–785. DOI: <https://doi.org/10.1091/mbc.E14-05-1019>
- Guo S**, Stolz LE, Lemrow SM, York JD. 1999. SAC1-like domains of yeast SAC1, INP52, and INP53 and of human synaptojanin encode polyphosphoinositide phosphatases. *Journal of Biological Chemistry* **274**:12990–12995. DOI: <https://doi.org/10.1074/jbc.274.19.12990>
- Haucke V**, Neher E, Sigrist SJ. 2011. Protein scaffolds in the coupling of synaptic exocytosis and endocytosis. *Nature Reviews Neuroscience* **12**:127–138. DOI: <https://doi.org/10.1038/nrn2948>, PMID: 21304549
- Heerssen H**, Fetter RD, Davis GW. 2008. Clathrin dependence of synaptic-vesicle formation at the *Drosophila* neuromuscular junction. *Current Biology* **18**:401–409. DOI: <https://doi.org/10.1016/j.cub.2008.02.055>, PMID: 18356056
- Heuser JE**, Reese TS. 1973. Evidence for recycling of synaptic vesicle membrane during transmitter release at the frog neuromuscular junction. *Journal of Cell Biology* **57**:315–344. DOI: <https://doi.org/10.1083/jcb.57.2.315>
- Hille B**, Dickson EJ, Kruse M, Vivas O, Suh B-C. 2015. Phosphoinositides regulate ion channels. *Biochimica Et Biophysica Acta (BBA) - Molecular and Cell Biology of Lipids* **1851**:844–856. DOI: <https://doi.org/10.1016/j.bbalip.2014.09.010>
- Holt M**, Cooke A, Wu MM, Lagnado L. 2003. Bulk membrane retrieval in the synaptic terminal of retinal bipolar cells. *The Journal of Neuroscience* **23**:1329–1339. DOI: <https://doi.org/10.1523/JNEUROSCI.23-04-01329.2003>, PMID: 12598621
- Honigsmann A**, van den Bogaart G, Iraheta E, Risselada HJ, Milovanovic D, Mueller V, Müller S, Diederichsen U, Fasshauer D, Grubmüller H, Hell SW, Eggeling C, Kühnel K, Jahn R. 2013. Phosphatidylinositol 4,5-bisphosphate clusters act as molecular beacons for vesicle recruitment. *Nature Structural & Molecular Biology* **20**:679–686. DOI: <https://doi.org/10.1038/nsmb.2570>, PMID: 23665582
- Hoopmann P**, Punge A, Barysch SV, Westphal V, Bückers J, Opazo F, Bethani I, Lauterbach MA, Hell SW, Rizzoli SO. 2010. Endosomal sorting of readily releasable synaptic vesicles. *PNAS* **107**:19055–19060. DOI: <https://doi.org/10.1073/pnas.1007037107>, PMID: 20956291
- Janmey PA**, Bucki R, Radhakrishnan R. 2018. Regulation of actin assembly by PI(4,5)P2 and other inositol phospholipids: an update on possible mechanisms. *Biochemical and Biophysical Research Communications* **506**:307–314. DOI: <https://doi.org/10.1016/j.bbrc.2018.07.155>, PMID: 30139519

- Jin YH, Wu XS, Shi B, Zhang Z, Guo X, Gan L, Chen Z, Wu LG. 2019. Protein kinase C and calmodulin serve as calcium sensors for Calcium-Stimulated endocytosis at synapses. *The Journal of Neuroscience* **39**:9478–9490. DOI: <https://doi.org/10.1523/JNEUROSCI.0182-19.2019>, PMID: 31628181
- Kabeche R, Madrid M, Cansado J, Moseley JB. 2015. Eisosomes Regulate Phosphatidylinositol 4,5-Bisphosphate (PI(4,5)P₂) Cortical Clusters and Mitogen-activated Protein (MAP) Kinase Signaling upon Osmotic Stress. *Journal of Biological Chemistry* **290**:25960–25973. DOI: <https://doi.org/10.1074/jbc.M115.674192>
- Kaempfer N, Maritzen T. 2017. Safeguards of neurotransmission: endocytic adaptors as regulators of synaptic vesicle composition and function. *Frontiers in Cellular Neuroscience* **11**:320. DOI: <https://doi.org/10.3389/fncel.2017.00320>, PMID: 29085282
- Kasprovicz J, Kuenen S, Miskiewicz K, Habets RLP, Smits L, Verstreken P. 2008. Inactivation of clathrin heavy chain inhibits synaptic recycling but allows bulk membrane uptake. *Journal of Cell Biology* **182**:1007–1016. DOI: <https://doi.org/10.1083/jcb.200804162>
- Khuong TM, Habets RL, Slabbaert JR, Verstreken P. 2010. WASP is activated by phosphatidylinositol-4,5-bisphosphate to restrict synapse growth in a pathway parallel to bone morphogenetic protein signaling. *PNAS* **107**:17379–17384. DOI: <https://doi.org/10.1073/pnas.1001794107>, PMID: 20844206
- Khuong TM, Habets RL, Kuenen S, Witkowska A, Kasprovicz J, Swerts J, Jahn R, van den Bogaart G, Verstreken P. 2013. Synaptic PI(3,4,5)P₃ is required for Syntaxin1A clustering and neurotransmitter release. *Neuron* **77**:1097–1108. DOI: <https://doi.org/10.1016/j.neuron.2013.01.025>, PMID: 23522045
- Kittelmann M, Liewald JF, Hegemann J, Schultheis C, Brauner M, Steuer Costa W, Wabnig S, Eimer S, Gottschalk A. 2013. In vivo synaptic recovery following optogenetic hyperstimulation. *PNAS* **110**:E3007–E3016. DOI: <https://doi.org/10.1073/pnas.1305679110>, PMID: 23878262
- Koh T-W, Korolchuk VI, Wairkar YP, Jiao W, Evergren E, Pan H, Zhou Y, Venken KJT, Shupliakov O, Robinson IM, O’Kane CJ, Bellen HJ. 2007. Eps15 and Dap160 control synaptic vesicle membrane retrieval and synapse development. *Journal of Cell Biology* **178**:309–322. DOI: <https://doi.org/10.1083/jcb.200701030>
- Kokotos AC, Peltier J, Davenport EC, Trost M, Cousin MA. 2018. Activity-dependent bulk endocytosis proteome reveals a key presynaptic role for the monomeric GTPase Rab11. *PNAS* **115**:E10177–E10186. DOI: <https://doi.org/10.1073/pnas.1809189115>, PMID: 30301801
- Kokotos AC, Low DW. 2015. Myosin II and dynamin control actin rings to mediate fission during activity-dependent bulk endocytosis. *Journal of Neuroscience* **35**:8687–8688. DOI: <https://doi.org/10.1523/JNEUROSCI.1172-15.2015>, PMID: 26063902
- Kononenko NL, Puchkov D, Classen GA, Walter AM, Pechstein A, Sawade L, Kaempfer N, Trimbuch T, Lorenz D, Rosenmund C, Maritzen T, Haucke V. 2014. Clathrin/AP-2 mediate synaptic vesicle reformation from endosome-like vacuoles but are not essential for membrane retrieval at central synapses. *Neuron* **82**:981–988. DOI: <https://doi.org/10.1016/j.neuron.2014.05.007>, PMID: 24908483
- Kononenko NL, Haucke V. 2015. Molecular mechanisms of presynaptic membrane retrieval and synaptic vesicle reformation. *Neuron* **85**:484–496. DOI: <https://doi.org/10.1016/j.neuron.2014.12.016>, PMID: 25654254
- Lam SS, Martell JD, Kamer KJ, Deerinck TJ, Ellisman MH, Mootha VK, Ting AY. 2015. Directed evolution of APEX2 for electron microscopy and proximity labeling. *Nature Methods* **12**:51–54. DOI: <https://doi.org/10.1038/nmeth.3179>
- Lee SY, Wenk MR, Kim Y, Nairn AC, De Camilli P. 2004. Regulation of synaptotagmin 1 by cyclin-dependent kinase 5 at synapses. *PNAS* **101**:546–551. DOI: <https://doi.org/10.1073/pnas.0307813100>, PMID: 14704270
- Lee SY, Voronov S, Letinic K, Nairn AC, Di Paolo G, De Camilli P. 2005. Regulation of the interaction between pipkiγ and talin by proline-directed protein kinases. *Journal of Cell Biology* **168**:789–799. DOI: <https://doi.org/10.1083/jcb.200409028>
- Levental I, Christian DA, Wang YH, Madara JJ, Discher DE, Janmey PA. 2009. Calcium-dependent lateral organization in phosphatidylinositol 4,5-bisphosphate (PIP₂)- and cholesterol-containing monolayers. *Biochemistry* **48**:8241–8248. DOI: <https://doi.org/10.1021/bi9007879>, PMID: 19630438
- Lou X. 2018. Sensing exocytosis and triggering endocytosis at synapses: synaptic vesicle Exocytosis-Endocytosis coupling. *Frontiers in Cellular Neuroscience* **12**:66. DOI: <https://doi.org/10.3389/fncel.2018.00066>, PMID: 29593500
- Mani M, Lee SY, Lucast L, Cremona O, Di Paolo G, De Camilli P, Ryan TA. 2007. The dual phosphatase activity of synaptotagmin1 is required for both efficient synaptic vesicle endocytosis and reavailability at nerve terminals. *Neuron* **56**:1004–1018. DOI: <https://doi.org/10.1016/j.neuron.2007.10.032>, PMID: 18093523
- Marks B, McMahon HT. 1998. Calcium triggers calcineurin-dependent synaptic vesicle recycling in mammalian nerve terminals. *Current Biology* **8**:740–749. DOI: [https://doi.org/10.1016/S0960-9822\(98\)70297-0](https://doi.org/10.1016/S0960-9822(98)70297-0), PMID: 9651678
- McMahon HT, Boucrot E. 2011. Molecular mechanism and physiological functions of clathrin-mediated endocytosis. *Nature Reviews Molecular Cell Biology* **12**:517–533. DOI: <https://doi.org/10.1038/nrm3151>, PMID: 21779028
- McPherson PS, Garcia EP, Slepnev VI, David C, Zhang X, Grabs D, Sossin WS, Bauerfeind R, Nemoto Y, De Camilli P. 1996. A presynaptic inositol-5-phosphatase. *Nature* **379**:353–357. DOI: <https://doi.org/10.1038/379353a0>, PMID: 8552192
- Miller TM, Heuser JE. 1984. Endocytosis of synaptic vesicle membrane at the frog neuromuscular junction. *Journal of Cell Biology* **98**:685–698. DOI: <https://doi.org/10.1083/jcb.98.2.685>
- Milosevic I, Giovedi S, Lou X, Raimondi A, Collesi C, Shen H, Paradise S, O’Toole E, Ferguson S, Cremona O, De Camilli P. 2011. Recruitment of endophilin to clathrin-coated pit necks is required for efficient vesicle uncoating after fission. *Neuron* **72**:587–601. DOI: <https://doi.org/10.1016/j.neuron.2011.08.029>, PMID: 22099461

- Morton A**, Marland JR, Cousin MA. 2015. Synaptic vesicle exocytosis and increased cytosolic calcium are both necessary but not sufficient for activity-dependent bulk endocytosis. *Journal of Neurochemistry* **134**:405–415. DOI: <https://doi.org/10.1111/jnc.13132>, PMID: 25913068
- Mu L**, Tu Z, Miao L, Ruan H, Kang N, Hei Y, Chen J, Wei W, Gong F, Wang B, Du Y, Ma G, Amerein MW, Xia T, Shi Y. 2018. A phosphatidylinositol 4,5-bisphosphate redistribution-based sensing mechanism initiates a phagocytosis programing. *Nature Communications* **9**:4259. DOI: <https://doi.org/10.1038/s41467-018-06744-7>, PMID: 30323235
- Nakano-Kobayashi A**, Yamazaki M, Unoki T, Hongu T, Murata C, Taguchi R, Katada T, Frohman MA, Yokozeki T, Kanaho Y. 2007. Role of activation of PIP5Kgamma661 by AP-2 complex in synaptic vesicle endocytosis. *The EMBO Journal* **26**:1105–1116. DOI: <https://doi.org/10.1038/sj.emboj.7601573>, PMID: 17290217
- Nguyen TH**, Maucort G, Sullivan RK, Schenning M, Lavidis NA, McCluskey A, Robinson PJ, Meunier FA. 2012. Actin- and dynamin-dependent maturation of bulk endocytosis restores neurotransmission following synaptic depletion. *PLOS ONE* **7**:e36913. DOI: <https://doi.org/10.1371/journal.pone.0036913>, PMID: 22629340
- Nicholson-Fish JC**, Kokotos AC, Gillingwater TH, Smillie KJ, Cousin MA. 2015. VAMP4 is an essential cargo molecule for Activity-Dependent bulk endocytosis. *Neuron* **88**:973–984. DOI: <https://doi.org/10.1016/j.neuron.2015.10.043>, PMID: 26607000
- Park J**, Cho OY, Kim JA, Chang S. 2016. Endosome-mediated endocytic mechanism replenishes the majority of synaptic vesicles at mature CNS synapses in an activity-dependent manner. *Scientific Reports* **6**:31807. DOI: <https://doi.org/10.1038/srep31807>, PMID: 27534442
- Pauli A**, Althoff F, Oliveira RA, Heidmann S, Schuldiner O, Lehner CF, Dickson BJ, Nasmyth K. 2008. Cell-type-specific TEV protease cleavage reveals cohesin functions in *Drosophila* neurons. *Developmental Cell* **14**:239–251. DOI: <https://doi.org/10.1016/j.devcel.2007.12.009>, PMID: 18267092
- Picas L**, Viaud J, Schauer K, Vanni S, Hnia K, Fraiser V, Roux A, Bassereau P, Gaits-Iacovoni F, Payrastré B, Laporte J, Manneville JB, Goud B. 2014. BIN1/M-Amphiphysin2 induces clustering of phosphoinositides to recruit its downstream partner dynamin. *Nature Communications* **5**:5647. DOI: <https://doi.org/10.1038/ncomms6647>, PMID: 25487648
- Richards DA**, Guatimosim C, Betz WJ. 2000. Two endocytic recycling routes selectively fill two vesicle pools in frog motor nerve terminals. *Neuron* **27**:551–559. DOI: [https://doi.org/10.1016/S0896-6273\(00\)00065-9](https://doi.org/10.1016/S0896-6273(00)00065-9), PMID: 11055437
- Richards DA**, Rizzoli SO, Betz WJ. 2004. Effects of wortmannin and latrunculin A on slow endocytosis at the frog neuromuscular junction. *The Journal of Physiology* **557**:77–91. DOI: <https://doi.org/10.1113/jphysiol.2004.062158>, PMID: 15004214
- Riggi M**, Niewola-Staszewska K, Chiaruttini N, Colom A, Kusmider B, Mercier V, Soleimanpour S, Stahl M, Matile S, Roux A, Loewith R. 2018. Decrease in plasma membrane tension triggers PtdIns(4,5)P₂ phase separation to inactivate TORC₂. *Nature Cell Biology* **20**:1043–1051. DOI: <https://doi.org/10.1038/s41556-018-0150-z>, PMID: 30154550
- Saheki Y**, De Camilli P. 2012. Synaptic Vesicle Endocytosis. *Cold Spring Harbor Perspectives in Biology* **4**:a005645. DOI: <https://doi.org/10.1101/cshperspect.a005645>
- Sarmiento MJ**, Coutinho A, Fedorov A, Prieto M, Fernandes F. 2014. Ca²⁺ induces PI(4,5)P₂ clusters on lipid bilayers at physiological PI(4,5)P₂ and Ca²⁺ concentrations. *Biochimica et Biophysica Acta (BBA) - Biomembranes* **1838**:822–830. DOI: <https://doi.org/10.1016/j.bbamem.2013.11.020>
- Silm K**, Yang J, Marcott PF, Asensio CS, Eriksen J, Guthrie DA, Newman AH, Ford CP, Edwards RH. 2019. Synaptic vesicle recycling pathway determines neurotransmitter content and release properties. *Neuron* **102**:786–800. DOI: <https://doi.org/10.1016/j.neuron.2019.03.031>
- Söderberg O**, Leuchowius KJ, Gullberg M, Jarvius M, Weibrecht I, Larsson LG, Landegren U. 2008. Characterizing proteins and their interactions in cells and tissues using the in situ proximity ligation assay. *Methods* **45**:227–232. DOI: <https://doi.org/10.1016/j.ymeth.2008.06.014>, PMID: 18620061
- Soykan T**, Kaempf N, Sakaba T, Vollweiter D, Goerdeler F, Puchkov D, Kononenko NL, Haucke V. 2017. Synaptic vesicle endocytosis occurs on multiple timescales and is mediated by Formin-Dependent actin assembly. *Neuron* **93**:854–866. DOI: <https://doi.org/10.1016/j.neuron.2017.02.011>, PMID: 28231467
- Stevens RJ**, Akbergenova Y, Jorquera RA, Littleton JT. 2012. Abnormal synaptic vesicle biogenesis in *Drosophila* synaptogyrin mutants. *Journal of Neuroscience* **32**:18054–18067. DOI: <https://doi.org/10.1523/JNEUROSCI.2668-12.2012>, PMID: 23238721
- Suh BC**, Hille B. 2008. PIP₂ is a necessary cofactor for ion channel function: how and why? *Annual Review of Biophysics* **37**:175–195. DOI: <https://doi.org/10.1146/annurev.biophys.37.032807.125859>, PMID: 18573078
- Sun T**, Wu XS, Xu J, McNeil BD, Pang ZP, Yang W, Bai L, Qadri S, Molkentin JD, Yue DT, Wu LG. 2010. The role of calcium/calmodulin-activated calcineurin in rapid and slow endocytosis at central synapses. *Journal of Neuroscience* **30**:11838–11847. DOI: <https://doi.org/10.1523/JNEUROSCI.1481-10.2010>, PMID: 20810903
- Traub LM**, Bonifacino JS. 2013. Cargo recognition in clathrin-mediated endocytosis. *Cold Spring Harbor Perspectives in Biology* **5**:a016790. DOI: <https://doi.org/10.1101/cshperspect.a016790>, PMID: 24186068
- Tsujishita Y**, Guo S, Stolz LE, York JD, Hurley JH. 2001. Specificity determinants in phosphoinositide dephosphorylation: crystal structure of an archetypal inositol polyphosphate 5-phosphatase. *Cell* **105**:379–389. DOI: [https://doi.org/10.1016/s0092-8674\(01\)00326-9](https://doi.org/10.1016/s0092-8674(01)00326-9), PMID: 11348594
- van den Bogaart G**, Meyenberg K, Risselada HJ, Amin H, Willig KI, Hubrich BE, Dier M, Hell SW, Grubmüller H, Diederichsen U, Jahn R. 2011. Membrane protein sequestering by ionic protein-lipid interactions. *Nature* **479**:552–555. DOI: <https://doi.org/10.1038/nature10545>, PMID: 22020284

- van den Bout I, Divecha N. 2009. PIP5K-driven PtdIns(4,5)P₂ synthesis: regulation and cellular functions. *Journal of Cell Science* **122**:3837–3850. DOI: <https://doi.org/10.1242/jcs.056127>, PMID: 19889969
- Verstreken P, Koh TW, Schulze KL, Zhai RG, Hiesinger PR, Zhou Y, Mehta SQ, Cao Y, Roos J, Bellen HJ. 2003. Synaptojanin is recruited by endophilin to promote synaptic vesicle uncoating. *Neuron* **40**:733–748. DOI: [https://doi.org/10.1016/S0896-6273\(03\)00644-5](https://doi.org/10.1016/S0896-6273(03)00644-5), PMID: 14622578
- Verstreken P, Ohyama T, Haueter C, Habets RL, Lin YQ, Swan LE, Ly CV, Venken KJ, De Camilli P, Bellen HJ. 2009. Tweek, an evolutionarily conserved protein, is required for synaptic vesicle recycling. *Neuron* **63**:203–215. DOI: <https://doi.org/10.1016/j.neuron.2009.06.017>, PMID: 19640479
- Vijayakrishnan N, Woodruff EA, Broadie K. 2009. Rolling blackout is required for bulk endocytosis in non-neuronal cells and neuronal synapses. *Journal of Cell Science* **122**:114–125. DOI: <https://doi.org/10.1242/jcs.036673>, PMID: 19066280
- Wagh DA, Rasse TM, Asan E, Hofbauer A, Schwenkert I, Dürrbeck H, Buchner S, Dabauvalle M-C, Schmidt M, Qin G, Wichmann C, Kittel R, Sigrist SJ, Buchner E. 2006. Bruchpilot, a protein with homology to ELKS/CAST, is required for structural integrity and function of synaptic active zones in *Drosophila*. *Neuron* **49**:833–844. DOI: <https://doi.org/10.1016/j.neuron.2006.02.008>
- Wang Y-H, Collins A, Guo L, Smith-Dupont KB, Gai F, Svitkina T, Janmey PA. 2012. Divalent Cation-Induced cluster formation by polyphosphoinositides in model membranes. *Journal of the American Chemical Society* **134**:3387–3395. DOI: <https://doi.org/10.1021/ja208640t>
- Watanabe S, Liu Q, Davis MW, Hollopeter G, Thomas N, Jorgensen NB, Jorgensen EM. 2013a. Ultrafast endocytosis at *Caenorhabditis elegans* neuromuscular junctions. *eLife* **2**:e00723. DOI: <https://doi.org/10.7554/eLife.00723>, PMID: 24015355
- Watanabe S, Rost BR, Camacho-Pérez M, Davis MW, Söhl-Kielczynski B, Rosenmund C, Jorgensen EM. 2013b. Ultrafast endocytosis at mouse hippocampal synapses. *Nature* **504**:242–247. DOI: <https://doi.org/10.1038/nature12809>, PMID: 24305055
- Wen Y, Vogt VM, Feigenson GW. 2018. Multivalent Cation-Bridged PI(4,5)P₂ Clusters Form at Very Low Concentrations. *Biophysical Journal* **114**:2630–2639. DOI: <https://doi.org/10.1016/j.bpj.2018.04.048>
- Wenk MR, Pellegrini L, Klenchin VA, Di Paolo G, Chang S, Daniell L, Arioka M, Martin TF, De Camilli P. 2001. PIP kinase $\text{ig}\gamma$ is the major PI(4,5)P₂ synthesizing enzyme at the synapse. *Neuron* **32**:79–88. DOI: [https://doi.org/10.1016/S0896-6273\(01\)00456-1](https://doi.org/10.1016/S0896-6273(01)00456-1), PMID: 11604140
- Wenzel EM, Morton A, Ebert K, Welzel O, Kornhuber J, Cousin MA, Groemer TW. 2012. Key physiological parameters dictate triggering of activity-dependent bulk endocytosis in hippocampal synapses. *PLOS ONE* **7**:e38188. DOI: <https://doi.org/10.1371/journal.pone.0038188>, PMID: 22675521
- Wilder EL. 2000. Ectopic expression in *Drosophila*. *Methods in Molecular Biology* **137**:9–14. DOI: <https://doi.org/10.1385/1-59259-066-7:9>, PMID: 10948520
- Winther AME, Jiao W, Vorontsova O, Rees KA, Koh T-W, Sopova E, Schulze KL, Bellen HJ, Shupliakov O. 2013. The dynamin-binding domains of Dap160/intersectin affect bulk membrane retrieval in synapses. *Journal of Cell Science* **126**:1021–1031. DOI: <https://doi.org/10.1242/jcs.118968>
- Wong CO, Chen K, Lin YQ, Chao Y, Duraine L, Lu Z, Yoon WH, Sullivan JM, Broadhead GT, Sumner CJ, Lloyd TE, Macleod GT, Bellen HJ, Venkatachalam K. 2014. A TRPV channel in *Drosophila* motor neurons regulates presynaptic resting Ca²⁺ levels, synapse growth, and synaptic transmission. *Neuron* **84**:764–777. DOI: <https://doi.org/10.1016/j.neuron.2014.09.030>, PMID: 25451193
- Woscholski R, Finan PM, Radley E, Totty NF, Sterling AE, Hsuan JJ, Waterfield MD, Parker PJ. 1997. Synaptojanin is the major constitutively active Phosphatidylinositol-3,4,5-trisphosphate 5-Phosphatase in rodent brain. *Journal of Biological Chemistry* **272**:9625–9628. DOI: <https://doi.org/10.1074/jbc.272.15.9625>
- Wu XS, McNeil BD, Xu J, Fan J, Xue L, Melicoff E, Adachi R, Bai L, Wu LG. 2009. Ca²⁺ and calmodulin initiate all forms of endocytosis during depolarization at a nerve terminal. *Nature Neuroscience* **12**:1003–1010. DOI: <https://doi.org/10.1038/nn.2355>, PMID: 19633667
- Wu LG, Hamid E, Shin W, Chiang HC. 2014a. Exocytosis and endocytosis: modes, functions, and coupling mechanisms. *Annual Review of Physiology* **76**:301–331. DOI: <https://doi.org/10.1146/annurev-physiol-021113-170305>, PMID: 24274740
- Wu XS, Zhang Z, Zhao WD, Wang D, Luo F, Wu LG. 2014b. Calcineurin is universally involved in Vesicle endocytosis at neuronal and nonneuronal secretory cells. *Cell Reports* **7**:982–988. DOI: <https://doi.org/10.1016/j.celrep.2014.04.020>, PMID: 24835995
- Wu Y, O'Toole ET, Girard M, Ritter B, Messa M, Liu X, McPherson PS, Ferguson SM, De Camilli P. 2014c. A dynamin 1-, dynamin 3- and clathrin-independent pathway of synaptic vesicle recycling mediated by bulk endocytosis. *eLife* **3**:e01621. DOI: <https://doi.org/10.7554/eLife.01621>, PMID: 24963135
- Wu X-S, Lee SH, Sheng J, Zhang Z, Zhao W-D, Wang D, Jin Y, Charnay P, Ervasti JM, Wu L-G. 2016. Actin Is Crucial for All Kinetically Distinguishable Forms of Endocytosis at Synapses. *Neuron* **92**:1020–1035. DOI: <https://doi.org/10.1016/j.neuron.2016.10.014>
- Wu W, Wu LG. 2007. Rapid bulk endocytosis and its kinetics of fission pore closure at a central synapse. *PNAS* **104**:10234–10239. DOI: <https://doi.org/10.1073/pnas.0611512104>, PMID: 17551019
- Xue J, Graham ME, Novelle AE, Sue N, Gray N, McNiven MA, Smillie KJ, Cousin MA, Robinson PJ. 2011. Calcineurin Selectively Docks with the Dynamin Ixb Splice Variant to Regulate Activity-dependent Bulk Endocytosis. *Journal of Biological Chemistry* **286**:30295–30303. DOI: <https://doi.org/10.1074/jbc.M111.273110>
- Yao CK, Lin YQ, Ly CV, Ohyama T, Haueter CM, Moiseenkova-Bell VY, Wensel TG, Bellen HJ. 2009. A synaptic vesicle-associated Ca²⁺ channel promotes endocytosis and couples exocytosis to endocytosis. *Cell* **138**:947–960. DOI: <https://doi.org/10.1016/j.cell.2009.06.033>, PMID: 19737521

- Yao CK**, Liu YT, Lee IC, Wang YT, Wu PY. 2017. A Ca²⁺ channel differentially regulates Clathrin-mediated and activity-dependent bulk endocytosis. *PLoS Biology* **15**:e2000931. DOI: <https://doi.org/10.1371/journal.pbio.2000931>, PMID: 28414717
- Zhu Y**, Xu J, Heinemann SF. 2009. Two pathways of synaptic vesicle retrieval revealed by single-vesicle imaging. *Neuron* **61**:397–411. DOI: <https://doi.org/10.1016/j.neuron.2008.12.024>, PMID: 19217377

Appendix 1

key resources table

Appendix 1—key resources table

Reagent type (species) or resource	Designation	Source or reference	Identifiers	Additional information
Genetic reagent (<i>D. melanogaster</i>)	<i>fwe</i> ^{DB25}	Yao et al., 2009		<i>fwe</i> mutant allele used in Figures 3–6, Figure 4—figure supplements 1–2, Figure 5—figure supplement 1 , and Figure 6—figure supplement 1
Genetic reagent (<i>D. melanogaster</i>)	<i>fwe</i> ^{DB56}	Yao et al., 2009		<i>fwe</i> mutant allele used in Figures 3–6, Figure 4—figure supplements 1–2, Figure 5—figure supplement 1 , and Figure 6—figure supplement 1
Genetic reagent (<i>D. melanogaster</i>)	UAS-Flag-Fwe-HA	Yao et al., 2017		Wild-type version of <i>fwe</i> transgene used in Figure 3a–b, Figure 6a, Figure 4—figure supplement 1 , and Figure 6—figure supplement 1b
Genetic reagent (<i>D. melanogaster</i>)	UAS-Flag-Fwe[E79Q]-HA	Yao et al., 2017		Channel deficient version of <i>fwe</i> transgene used in Figure 3e–f
Genetic reagent (<i>D. melanogaster</i>)	UAS- <i>canA1</i> -RNAi (FB4)	Dijkers and O'Farrell, 2007		RNAi line of <i>canA1</i> used in Figure 3g–j
Genetic reagent (<i>D. melanogaster</i>)	UAS- <i>canA1</i> -RNAi(TRiP.JF01871)	Bloomington <i>Drosophila</i> Stock Center Dijkers and O'Farrell, 2007	RRID:BDSC_25850	RNAi line of <i>canA1</i> used in Figure 3g–h, 5
Genetic reagent (<i>D. melanogaster</i>)	UAS- <i>synj</i>	Khuong et al., 2013		Wild-type version of <i>synj</i> transgene used in Figure 2b–d, Figure 3i–j, Figure 6d–f , and Figure 1—figure supplement 1c .
Genetic reagent (<i>D. melanogaster</i>)	UAS-PLC _{δ1} -PH-EGFP	Bloomington <i>Drosophila</i> Stock Center Verstreken et al., 2009	RRID:BDSC_39693	PI(4,5)P ₂ reporter transgene used in Figures 1–4, Figure 1—figure supplement 1, Figure 1—figure supplement 3c, Figure 2—figure supplements 1–2, Figure 4—figure supplement 1e–f .
Genetic reagent (<i>D. melanogaster</i>)	UAS-PLC _{δ1} -PHS39R-EGFP	Bloomington <i>Drosophila</i> Stock Center Verstreken et al., 2009	RRID:BDSC_39694	PI(4,5)P ₂ -binding mutant transgene used in Figure 2c–d, Figure 1—figure supplement 2c–e

Continued on next page

Appendix 1—key resources table continued

Reagent type (species) or resource	Designation	Source or reference	Identifiers	Additional information
Genetic reagent (D. <i>melanogaster</i>)	<i>nSyb-GAL4</i>	Bloomington <i>Drosophila</i> Stock Center Pauli et al., 2008	RRID:BDSC_51635	Neuronal GAL4 driver used in all figures
Genetic reagent (D. <i>melanogaster</i>)	<i>vglut-lexA</i>	Bloomington <i>Drosophila</i> Stock Center	RRID:BDSC_60314	Motor neuron <i>lexA</i> driver used in Figure 3e–f , Figure 3i–j , Figure 4d–e , and Figure 4—figure supplement 1c–d
Genetic reagent (D. <i>melanogaster</i>)	13XLexAop2-IVS-GCaMP6f	Bloomington <i>Drosophila</i> Stock Center	RRID:BDSC_44277	Ca ²⁺ indicator transgene used in Figure 3i–j , Figure 4d–e , and Figure 4—figure supplement 1c–d
Genetic reagent (D. <i>melanogaster</i>)	<i>synj</i> ¹	Bloomington <i>Drosophila</i> Stock Center Verstreken et al., 2003	RRID:BDSC_24883	<i>synj</i> mutant allele used in Figure 1—figure supplement 1c–d
Genetic reagent (D. <i>melanogaster</i>)	UAS- <i>mCD8-EGFP</i>	Kyoto Stock Center	RRID:DGRC_108068	<i>mCD8-EGFP</i> transgene used in Figure 1—figure supplement 2a–b
Genetic reagent (D. <i>melanogaster</i>)	UAS-HA-Fwe[WT]-APEX2	This paper		APEX2 fusion version of wild-type <i>fwe</i> transgene used in Figure 4d–g , Figure 5 , Figure 6b–f , Figure 4—figure supplement 2 , and Figure 6—figure supplement 1c–d
Genetic reagent (D. <i>melanogaster</i>)	UAS-HA-Fwe[K29A/R33A]-APEX2	This paper		APEX2 fusion version of <i>fwe</i> [K29A/R33A] transgene used in Figure 4d–g , Figure 5 , Figure 4—figure supplement 2
Genetic reagent (D. <i>melanogaster</i>)	UAS-Flag-Fwe[K29A/R33A/K95A/K100A/R105A/K146A/K147A/R150A]-HA	This paper		<i>fwe</i> [K29A/R33A/K95A/K100A/R105A/K146A/K147A/R150A] transgene was not expressed stably
Genetic reagent (D. <i>melanogaster</i>)	UAS-Flag-Fwe[K146A/K147A/R150A]-HA	This paper		<i>fwe</i> [K146A/K147A/R150A] transgene used in Figure 4—figure supplement 1
Genetic reagent (D. <i>melanogaster</i>)	UAS-Flag-Fwe[K95A/K100A/R105A]-HA	This paper		<i>fwe</i> [K95A/K100A/R105A] transgene was not expressed stably
Genetic reagent (D. <i>melanogaster</i>)	LexAop2-PLC δ_1 -PH-APEX2-HA	This paper		APEX2 fusion version of PLC δ_1 -PH transgene used in Figure 3i–j
Genetic reagent (D. <i>melanogaster</i>)	LexAop2-PLC δ_1 -PH-EGFP	This paper		<i>lexAop2</i> version of PLC δ_1 -PH-EGFP transgene used in Figure 3e–f
Antibody	α -GFP (Chicken polyclonal)	Invitrogen	Cat #A10262, RRID: AB_2534023	IF: 1:500 WB: 1:5000
Antibody	α -HA (Mouse monoclonal)	Sigma	Cat # H3663, RRID: AB_262051	IF: 1:400 PLA: 1:200

Continued on next page

Appendix 1—key resources table continued

Reagent type (species) or resource	Designation	Source or reference	Identifiers	Additional information
Antibody	α -Bruchpilot (Mouse monoclonal)	DSHB Wagh et al., 2006	Cat# nc82, RRID:AB_2314866	IF: 1:100
Antibody	α -AP-2 α (Rabbit polyclonal)	González-Gaitán and Jäckle, 1997		IF: 1:3000
Antibody	α -Eps15 (Guinea pig polyclonal)	Koh et al., 2007		IF: 1:3000
Antibody	α -Fwe B isoform (Guinea pig polyclonal)	Yao et al., 2017		IF: 1:400
Antibody	Cy3 AffiniPure Rabbit Anti-Horseradish Peroxidase	Jackson Immuno Research Labs	Cat# 323-165-021, RRID:AB_2340262	IF: 1:250
Antibody	Alexa Fluor 488 AffiniPure Rabbit Anti-Horseradish Peroxidase	Jackson Immuno Research Labs	Cat# 323-545-021, RRID:AB_2340264	IF: 1:250
Antibody	α -GFP (Rabbit polyclonal)	Thermo Fisher Scientific	Cat# A-6455, RRID:AB_221570	PLA: 1:500
Antibody	α -actin (Mouse monoclonal)	Sigma	Cat# A7732, RRID:AB_2221571	WB:1:20000
Antibody	α -1D4 (Mouse monoclonal)	Yao et al., 2009		WB: 1:2000
Strain, strain background (<i>Escherichia coli</i>)	DH5 α			
Strain, strain background (<i>Escherichia coli</i>)	yeast strain BJ5457	Yao et al., 2009		
Peptide, recombinant protein	Nluc-Fwe-1D4 fusion protein	This paper		Used in Figure 4b–c
Peptide, recombinant protein	Nluc-Fwe[K29A/R33A]–1D4	This paper		Used in Figure 4b–c
Peptide, recombinant protein	Nluc-Fwe[K95A/K100A/R105A/K146A/K147/R150A]–1D4	This paper		Used in Figure 4b–c
Peptide, recombinant protein	Nluc-Fwe[K29A/R33A/K95A/K100A/R105A/K146A/K147A/R150A]–1D4	This paper		Used in Figure 4b–c
Chemical compound, drug	n-Dodecyl- β -D-Maltopyranoside	Anatrace	Cat# D310	Used in Figure 4b–c
Chemical compound, drug	BODIPY-TMR Phosphatidylinositol 4,5-bisphosphate	Echelon Bioscience	Cat#C-45M16A	Used in Figure 4b–c
Chemical compound, drug	Furimazine	Promega	Cat# N1110	Used in Figure 4b–c

Continued on next page

Appendix 1—key resources table continued

Reagent type (species) or resource	Designation	Source or reference	Identifiers	Additional information
Chemical compound, drug	Brain Phosphatidylinositol 4,5-bisphosphate	Avanti Polar Lipids	AV-840046P	Used in Figure 4b–c
Commercial assay or kit	Duolink In Situ Red Starter Kit Mouse/Rabbit	Sigma	Cat# DUO92101	Used in Figure 3a–b
Commercial assay or kit	NEBuilder HiFi DNA Assembly Master Mix	NEB	Cat# E2621	
Recombinant DNA reagent	YeMP	Yao et al., 2009		
Recombinant DNA reagent	pcDNA3 APEX2-NES	Addgene	RRID:Addgene_49386	
Recombinant DNA reagent	pJFRC19-13XLexAop2-IVS-myr:GFP	Addgene	RRID:Addgene_26224	
Recombinant DNA reagent	pNL1.1[Nluc]	Promega	Cat# #N1001	
Recombinant DNA reagent	pUAST-HA-Fwe[WT]-APEX2	This paper		DNA construct of APEX2 fusion version of wild-type fwe transgene used in Figure 4d–g, Figure 5, Figure 6b–f, Figure 4—figure supplement 2, and Figure 6—figure supplement 1c–d
Recombinant DNA reagent	pUAST-HA-Fwe[K29A/R33A]-APEX2	This paper		DNA construct of APEX2 fusion version of fwe[K29A/R33A] transgene used in Figure 4d–g, Figure 5, Figure 4—figure supplement 2
Recombinant DNA reagent	pUAST-Flag-Fwe-HA	Yao et al., 2017		
Recombinant DNA reagent	pUAST-Flag-Fwe[K29/R33/K95/K100/R105/K146A/K147A/R150A]-HA	This paper		DNA construct of fwe[K29A/R33A/K95A/K100A/R105A/K146A/K147A/R150A] transgene
Recombinant DNA reagent	pUAST-Flag-Fwe[K146A/K147A/R150A]-HA	This paper		DNA construct of fwe[K146A/K147A/R150A] transgene used in Figure 4—figure supplement 1
Recombinant DNA reagent	pUAST-Flag-Fwe[K95/K100/R105A]-HA	This paper		DNA construct of fwe[K95A/K100A/R105A] transgene
Recombinant DNA reagent	plexAop2-PLC δ ₁ -PH-APEX2-HA	This paper		DNA construct of APEX2 fusion version of PLC δ ₁ -PH transgene used in Figure 3i–j
Recombinant DNA reagent	plexAop2-PLC δ ₁ -PH-EGFP	This paper		DNA construct of lexAop2 version of PLC δ ₁ -PH-EGFP transgene used in Figure 3e–f

Continued on next page

Appendix 1—key resources table continued

Reagent type (species) or resource	Designation	Source or reference	Identifiers	Additional information
Recombinant DNA reagent	YeMP-Nluc-Fwe-1D4	This paper		DNA construct of expression of Nluc-Fwe-1D4 recombinant protein used in Figure 4b–c
Recombinant DNA reagent	YeMP-Nluc-Fwe[K29A/R33A]–1D4	This paper		DNA construct of expression of Nluc-Fwe[K29A/R33A]–1D4 recombinant protein used in Figure 4b–c
Recombinant DNA reagent	YeMP-Nluc-Fwe[K95A/K100A/R105A/K146A/K147/R150A]–1D4	This paper		DNA construct of expression of Nluc-Fwe[K95A/K100A/R105A/K146A/K147/R150A]–1D4 recombinant protein used in Figure 4b–c
Recombinant DNA reagent	YeMP-Nluc-Fwe[K29A/R33A/K95A/K100A/R105A/K146A/K147A/R150A]–1D4	This paper		DNA construct of expression of Nluc-Fwe[K29A/R33A/K95A/K100A/R105A/K146A/K147A/R150A]–1D4 recombinant protein used in Figure 4b–c
Sequence-based reagent	HA-Fwe[WT]-APEX2 forward-1	This paper		5'-tcgtaacagatcttGCGGCCGCA T GTACCCATACGATG TTCCAGATTACG-3'
Sequence-based reagent	HA-Fwe[WT]-APEX2 Reverse-1	This paper		5'- tgaacctctccgccTGT GGGGCGCCAGACATC-3'
Sequence-based reagent	HA-Fwe[WT]-APEX2 forward-2	This paper		5'- gccccacaggcggaggaggttca ggaggcggaggttcgGG TACCGG CGGAAAGAGTTACCCGAC- 3'
Sequence-based reagent	HA-Fwe[WT]-APEX2 Reverse-2	This paper		5'- tccttcacaaagatccTCTAGAG GCGTCGGCGAATCCCAG –3'
Sequence-based reagent	HA-Fwe[K29A/R33A]-APEX2-HA forward	This paper		5'-CAGCCGTGGTATC TCGCA TATGGAAGTGCATTGC TGGCATTG-3'
Sequence-based reagent	Flag-Fwe[K95/K100/R105A]-HA forward	This paper		5'-GGAATCTGCGCCCTTG TACTT CGCTGCCGGGTCTACA TTGCC ATGGCCATTCCGCCATTA TT-3'
Sequence-based reagent	Flag-Fwe[K146A/K147A/R150A]-HA forward	This paper		5'-CAGAGGACA TGGCCGCCGC TGCCACA TCGCCACACAGATG GCCGGCAG TCAGGCGGGCGG-3'
Sequence-based reagent	PLC δ ₁ -PH-APEX2-HA forward-1	This paper		5'-tcttatccttacttcagCGCGC CGCATGGAC TCGGGCCGGGAC-3'

Continued on next page

Appendix 1—key resources table continued

Reagent type (species) or resource	Designation	Source or reference	Identifiers	Additional information
Sequence-based reagent	PLC _{δ1} -PH-APEX2-HA forward-2	This paper		5'- GCTGTACAAG ggcggaggaggttca ggaggcggagggttcgGGCGGAA AGAGTTACCCGAC-3'
Sequence-based reagent	PLC _{δ1} -PH-APEX2-HA reverse-1	This paper		5'- cctccgccgtaccAAGATCT TCCGGGCATAGCTGTGCG-3'
Sequence-based reagent	PLC _{δ1} -PH-APEX2-HA reverse-2	This paper		5'- ggttccttcacaaagatcctctagattaa gcgtaatctggaacatcgatgggtaG GCGTCGGCAATCCAG -3'
Sequence-based reagent	PLC _{δ1} -PH-EGFP forward	This paper		5'- tcttctcttactcagGCGGCC GCATGGAC TCGGGCCGGGAC-3'
Sequence-based reagent	PLC _{δ1} -PH-EGFP reverse	This paper		5'- TTTCTAGATTACTTG TACAGCTCGTCCAT-3'
Sequence-based reagent	YeMP-Nluc-Fwe-1D4 forward-1	This paper		5'- CCACTAGTATGGT CTTCACACTCGAAG-3'
Sequence-based reagent	YeMP-Nluc-Fwe-1D4 forward-2	This paper		5'- AAAACTAGTGTGCGAC TCGT TTGCGGAAAAGATAACG -3'
Sequence-based reagent	YeMP-Nluc-Fwe-1D4 Reverse-1	This paper		5'-AAAGTCGACCGA ACCTCCGCTCC-3'
Sequence-based reagent	YeMP-Nluc-Fwe-1D4 Reverse-2	This paper		5'- AAAACGCGTTTACG CAGGCGCGACTTGG-3'
Sequence-based reagent	YeMP-Nluc-Fwe[K29A/R33A]–1D4, YeMP-Nluc-Fwe[K95A/K100A/R105A/K146A/K147/R150A]–1D4, YeMP-Nluc-Fwe[K29A/R33A/K95A/K100A/R105A/K146A/K147A/R150A]–1D4 forward	This paper		5'- AAAACTAGTGTGCGAC TCG TTTGCGGAAAAGATAACG-3'
Sequence-based reagent	YeMP-Nluc-Fwe[K29A/R33A]–1D4, YeMP-Nluc-Fwe[K95A/K100A/R105A/K146A/K147/R150A]–1D4, YeMP-Nluc-Fwe[K29A/R33A/K95A/K100A/R105A/K146A/K147A/R150A]–1D4 Reverse	This paper		5'- AAAACGCG TTTACGCAGGCGCG ACTTGGCTGGTCTCTGTTG TGGGGCGCC-3'
Software, algorithm	LSM Zen	Zeiss	https://www.zeiss.com/microscopy/us/products/microscope-software/zen-lite.html	
Software, algorithm	Image J	https://imagej.net/contributors	https://imagej.nih.gov/ij/	

Continued on next page

Appendix 1—key resources table continued

Reagent type (species) or resource	Designation	Source or reference	Identifiers	Additional information
Software, algorithm	pClamp 10.6	Moleculardevices	https://www.moleculardevices.com/products/cellular-imaging-systems/acquisition-and-analysis-software/metamorph-microscopy#gref	
Software, algorithm	MetaMorph	Moleculardevices	https://www.moleculardevices.com/products/cellular-imaging-systems/acquisition-and-analysis-software/metamorph-microscopy#gref	
Software, algorithm	GraphPad Prism 8.0	Prism	https://www.graphpad.com/	